NASA TECHNICAL NOTE

NASA TN D-7637

NASA TN D-7637

APPLICATION OF BOUNDARY INTEGRAL METHOD TO ELASTOPLASTIC ANALYSIS OF V-NOTCHED BEAMS

by Walter Rzasnicki, Alexander Mendelson, Lynn U. Albers, and Demetrius D. Raftopoulos

Lewis Research Center
Cleveland, Ohio 44135

NATIONAL AERONAUTICS AND SPACE ADMINISTRATION • WASHINGTON, D. C. • APRIL 1974

1. Report No.	2. Government Accession No.	3. Recipient's Catalog No.
NASA TN D-7637		

4. Title and Subtitle	5. Report Date
APPLICATION OF BOUNDARY INTEGRAL METHOD TO ELASTOPLASTIC ANALYSIS OF V-NOTCHED BEAMS	APRIL 1974
	6. Performing Organization Code

7. Author(s)	8. Performing Organization Report No.
Walter Rzasnicki, Alexander Mendelson, Lynn U. Albers, and Demetrius D. Raftopoulos	E-7658
	10. Work Unit No. 501-21
9. Performing Organization Name and Address Lewis Research Center National Aeronautics and Space Administration Cleveland, Ohio 44135	11. Contract or Grant No.
	13. Type of Report and Period Covered Technical Note
12. Sponsoring Agency Name and Address National Aeronautics and Space Administration Washington, D.C. 20546	14. Sponsoring Agency Code

15. Supplementary Notes

16. Abstract

The boundary integral equation method was applied in the solution of the plane elastoplastic problem. The use of this method was illustrated by obtaining stress and strain distributions for a number of specimens with a single-edge notch and subjected to pure bending. The boundary integral equation method reduced the inhomogeneous biharmonic equation to two coupled Fredholm-type integral equations. These integral equations were replaced by a system of simultaneous algebraic equations and solved numerically in conjunction with a method of successive elastic solutions.

17. Key Words (Suggested by Author(s))		18. Distribution Statement
Fracture mechanics	Boundary integrals	Unclassified - unlimited
Stress-intensity factor	Plasticity	Category 32
J integral		

19. Security Classif. (of this report)	20. Security Classif. (of this page)	21. No. of Pages	22. Price*
Unclassified	Unclassified	43	$3.25

* For sale by the National Technical Information Service, Springfield, Virginia 22151

APPLICATION OF BOUNDARY INTEGRAL METHOD TO ELASTOPLASTIC ANALYSIS OF V-NOTCHED BEAMS

by Walter Rzasnicki, Alexander Mendelson, Lynn U. Albers, and Demetrius D. Raftopoulos*

Lewis Research Center

SUMMARY

The boundary integral equation method was applied in the solution of the plane elastoplastic problem. The use of this method was illustrated by obtaining stress and strain distributions for a number of specimens with a single edge notch and subjected to pure bending. The boundary integral equation method reduced the inhomogeneous biharmonic equation to two coupled Fredholm-type integral equations. These integral equations were replaced by a system of simultaneous algebraic equations and solved numerically in conjunction with a method of successive elastic solutions.

INTRODUCTION

Knowledge of the stress distribution in the neighborhood of a singularity, such as the tip of a V-notch in a bar loaded in tension or bending, is of fundamental importance in evaluating the resistance to fracture of structural materials. Elastic solutions to various geometries have been obtained by a number of different methods. Among the more effective ones, are the complex variable method (ref. 1), collocation method (ref. 2), and finite element method (ref. 3). However, the first two of these methods are not general enough nor readily adaptable to three-dimensional or elastoplastic problems. And the finite element method requires solutions of large sets of equations and fails to give sufficiently fine resolution in the vicinity of notch tips.

The recently developed boundary integral methods (ref. 4) offer an attractive alternative to other methods of analysis. These methods have a number of advantages as listed in references 4 and 5, the most important of which is that nodal points are needed

*Professor of Mechanical Engineering, University of Toledo, Toledo, Ohio.

only on the boundary instead of throughout the region as required by finite element methods. To date these methods have been used primarily for obtaining elastic solutions to various problems. Their extension to elastoplastic problems has been proposed in references 4 and 6. However, no elastoplastic solution has heretofore been obtained.

Reference 5 describes in detail the application of a boundary integral method to the solution of the elastic problem of a V-notched beam in pure bending. The present report extends this method to the more complicated elastoplastic problems. Solutions of such problems by finite elements has not been too successful in obtaining fine enough resolution and sufficiently accurate results in the vicinity of the notch tip (ref. 7). The present method overcomes these difficulties, since the stress and strain can be computed at any arbitrary point in the body from a knowledge of boundary values only.

SYMBOLS

A	area of cell in region R
$A_{ij}, B_{ij}, C_{ij}, D_{ij}$ $E_{ij}, F_{ij}, G_{ij}, H_{ij}$ I_{ij}, K_{ij}	coefficients in stress equations (14)
a	notch depth
a_{ij}, b_{ij}, c_{ij} d_{ij}, e_{ij}, f_{ij}	coefficients in boundary equations (10)
$\tilde{a}$	dimensionless notch depth, a/w
C	boundary contour
E	Young's modulus of elasticity
g	function of plastic strain increments
J	path independent contour integral
K_I	stress intensity factor for mode I
K_I^*	generalized stress intensity factor for mode I
L	half length of beam
m	strain hardening parameter, ratio of slope of linear strain-hardening curve to elastic modulus
n	order of stress singularity
$\bar{n}, \bar{s}$	unit vectors normal and tangent to contour C

$P(x, y)$	point on contour C or in region R
$q(\xi, \eta)$	point on contour C
$\tilde{q}$	dimensionless load, σ_{max}/σ_0
R	planar region bounded by closed contour C
r_{ij}	distance between two points having coordinates $(x, y)_i$ and $(\xi, \eta)_j$
r, θ	polar coordinates
s	length measured along contour C
T	convergence parameter
u_i	displacement vector
u_y	displacement in y direction
w	width of beam
x, y, z	rectangular Cartesian coordinates
$\tilde{x}, \tilde{y}$	dimensionless rectangular Cartesian coordinates, x/w, y/w
α	notch angle
∇^2	Laplace's operator, $\frac{\partial^2}{\partial x^2} + \frac{\partial^2}{\partial y^2}$
∇^4	biharmonic operator, $\frac{\partial^4}{\partial x^4} + 2\frac{\partial^4}{\partial x^2 \partial y^2} + \frac{\partial^4}{\partial y^4}$
δ_{ij}	Kronecker delta
ϵ_{ij}	strain tensor
ϵ_{et}	equivalent modified total strain
$\Delta\epsilon_p$	equivalent plastic strain increment
$\epsilon_x, \epsilon_y, \epsilon_z, \epsilon_{xy}$	components of strain tensor in Cartesian coordinates
ϵ'_{ij}	modified total strain tensor
$\epsilon'_x, \epsilon'_y, \epsilon'_z, \epsilon'_{xy}$	components of modified total strain tensor in Cartesian coordinates
μ	Poisson's ratio
ξ, η	rectangular Cartesian coordinates
ρ	function of r, $r^2 \ln r$
σ_e	equivalent stress
σ_{max}	maximum nominal bending stress

$\sigma_x, \sigma_y, \sigma_z, \sigma_{xy}$	components of stress tensor in Cartesian coordinates
σ_0	tensile yield stress
Φ	function of Airy stress function, $\nabla^2\varphi$
φ	Airy stress function
Subscript:	
i, j, k	integers
Superscripts:	
e	elastic
p	plastic
~	dimensionless quantity
'	derivative in outward normal direction, $\partial/\partial n$

METHOD OF SOLUTION

The problem of determining the state of stress and strain in a plane elastoplastic problem can be reduced to solving the following inhomogeneous biharmonic equation for the Airy stress function, as shown in reference 8:

$$\nabla^4\varphi = g(x, y) \tag{1}$$

$$g(x, y) = -\frac{E}{1 - \mu^2}\left[\frac{\partial^2}{\partial y^2}\left(\epsilon_x^p + \Delta\epsilon_y^p\right) + \frac{\partial^2}{\partial x^2}\left(\epsilon_y^p + \Delta\epsilon_y^p\right) - 2\frac{\partial^2}{\partial x\,\partial y}\left(\epsilon_{xy}^p + \Delta\epsilon_{xy}^p\right)\right]$$

$$+ \frac{\mu E}{1 - \mu^2}\nabla^2\left(\epsilon_x^p + \Delta\epsilon_x^p + \epsilon_y^p + \Delta\epsilon_y^p\right) \tag{2}$$

for the plane strain case and

$$g(x, y) = -E\left[\frac{\partial^2}{\partial y^2}\left(\epsilon_x^p + \Delta\epsilon_x^p\right) + \frac{\partial^2}{\partial x^2}\left(\epsilon_y^p + \Delta\epsilon_y^p\right) - 2\frac{\partial^2}{\partial x\,\partial y}\left(\epsilon_{xy}^p + \Delta\epsilon_{xy}^p\right)\right] \tag{3}$$

for the plane stress case, where, ϵ_x^p, ϵ_y^p, and ϵ_{xy}^p represent the accumulation of plastic strain increments from the beginning of the loading history up to, but not including the

current increment of the load, and $\Delta\epsilon_x^p$, $\Delta\epsilon_y^p$, and $\Delta\epsilon_{xy}^p$ are the increments of plastic strain due to the current increment of load.

The stress function φ must satisfy appropriate boundary conditions. For the problem under consideration (fig. 1), $\varphi(x, y)$ and its outward normal derivative $\partial\varphi/\partial n$ must satisfy the following boundary conditions (ref. 9):

$$\left.\begin{aligned}
&\varphi(x, y) = 0;\ \frac{\partial\varphi}{\partial n} = 0 \qquad \text{along boundary OA and OA'} \\
&\varphi(x, y) = 0;\ \frac{\partial\varphi}{\partial n} = 0 \qquad \text{along boundary AB and A'B'} \\
&\varphi(x, y) = -\frac{\sigma_{max}}{w}\left(\frac{x^3}{3} + ax^2 + a^2x + \frac{a^3}{3}\right) + \sigma_{max}\left(\frac{x^2}{2} + ax + \frac{a^2}{2}\right); \\
&\qquad\qquad \frac{\partial\varphi}{\partial n} = 0 \qquad \text{along boundary BC and B'C'} \\
&\varphi(x, y) = \frac{\sigma_{max} w^2}{6};\ \frac{\partial\varphi}{\partial n} = 0 \qquad \text{along boundary CD and C'D}
\end{aligned}\right\} \tag{4}$$

To solve equation (1) by means of the boundary integral method, use is made of Green's second theorem to reduce this equation to coupled integral equations, as shown in references 4 and 9. The result is

$$8\pi\varphi(x, y) - \iint_R \rho g(\xi, \eta)\, d\xi\, dn = \int_C \left[\varphi \frac{\partial}{\partial n}(\nabla^2\rho) - \frac{\partial\varphi}{\partial n}\nabla^2\rho + \Phi\frac{\partial\rho}{\partial n} - \frac{\partial\Phi}{\partial n}\rho\right] ds$$

$$\text{for } P \subset R \tag{5}$$

$$4\pi\varphi(x, y) - \iint_R \rho g(\xi, \eta)\, d\xi\, d\eta = \int_C \left[\varphi \frac{\partial}{\partial n}(\nabla^2\rho) - \frac{\partial\varphi}{\partial n}\nabla^2\rho + \Phi\frac{\partial\rho}{\partial n} - \frac{\partial\Phi}{\partial n}\rho\right] ds$$

$$\text{for } P \subset C \tag{6}$$

and

$$2\pi\Phi(x, y) - \iint_R g(\xi, \eta) \ln r \, d\xi \, d\eta = \int_C \left[\Phi \frac{\partial}{\partial n} (\ln r) - \frac{\partial \Phi}{\partial n} \ln r\right] ds \qquad \text{for } P \subset R \tag{7}$$

$$\pi\Phi(x, y) - \iint_R g(\xi, \eta) \ln r \, d\xi \, d\eta = \int_C \left[\Phi \frac{\partial}{\partial n} (\ln r) - \frac{\partial \Phi}{\partial n} \ln r\right] ds \qquad \text{for } P \subset C \tag{8}$$

where

$$\Phi \equiv \nabla^2 \varphi$$

$$\rho \equiv r^2 \ln r$$

and $r(x, y; \xi, \eta)$ is the distance between any two points $P(x, y)$ and $q(\xi, \eta)$ in the region R bounded by the curve C, such that $P \subset R + C$ and $q \subset C$ (fig. 2).

Equation (5) would, for a known function $g(x, y)$, give us directly a solution to the biharmonic equation (1) provided the functions $\varphi(x, y)$, $\partial\varphi(x, y)/\partial n$, $\nabla^2\varphi(x, y)$, and $\partial[\nabla^2\varphi(x, y)]/\partial n$ were known on the boundary C.

However, only the stress function φ and its outward normal derivative $\partial\varphi/\partial n$ are specified (eq. (4)). The values of $\nabla^2\varphi \equiv \Phi$ and $\partial(\nabla^2\varphi)/\partial n \equiv \partial\Phi/\partial n$ on the boundary must be compatible with the given values of φ and $\partial\varphi/\partial n$. To assure this compatibility, we have to solve the system of coupled integral equations (6) and (8), which contain the unknown functions Φ and $\partial\Phi/\partial n$.

Once the values of Φ and $\partial\Phi/\partial n$ on the boundary C of region R are known we can proceed with the calculation of the stress field in the region R utilizing equation (5) and the equations which define φ, namely,

$$\sigma_x = \frac{\partial^2 \varphi}{\partial y^2}, \qquad \sigma_y = \frac{\partial^2 \varphi}{\partial x^2}, \qquad \sigma_{xy} = -\frac{\partial^2 \varphi}{\partial x \, \partial y} \tag{9}$$

The calculation of the function $g(x, y)$, which is obtained iteratively, will be discussed subsequently.

NUMERICAL PROCEDURES

Solution of the Integral Equations

Since it is generally impossible to solve the system of coupled integral equations analytically, a numerical method is utilized in which the integral equations (6) and (8)

are replaced by a system of simultaneous algebraic equations.

For simplicity of notation the normal derivatives are denoted by prime superscripts. The boundary is divided into n intervals, not necessarily equal, numbered consecutively in the direction of increasing s. The center of each interval is designated as a node. The values of Φ and Φ' are assumed constant on each interval and equal to the values calculated at the node.

In similar manner the interior of region R is covered by a grid, containing m cells. The cells do not have to have equal areas. Their nodal points are located at the centroids. The value of $g(\xi, \eta)$ is assumed constant over each cell and equal to the value calculated at the centroid. The arrangement of boundary and interior subdivisions is shown in figures 3 and 4.

Using these assumptions, equations (6) and (8) can be replaced by a system of 2n simultaneous algebraic equations with 2n unknowns, that is, Φ_i and Φ_i'

$$\left.\begin{aligned} \pi\Phi_i - \sum_{k=1}^{m} \ln r_{ik}(gA)_k &= \sum_{j=1}^{n} (a_{ij}\Phi_j + b_{ij}\Phi_j') \\ 4\pi\varphi_i - \sum_{k=1}^{m} \rho_{ik}(gA)_k &= \sum_{j=1}^{n} (c_{ij}\Phi_j + d_{ij}\Phi_j' + e_{ij}\varphi_j + f_{ij}\varphi_j') \end{aligned}\right\} \tag{10}$$

where $i = 1, 2, 3, \ldots, n$, r_{ik} is the distance from i^{th} node to the centroid of the k^{th} cell, A_k is the area of the k^{th} cell, and

$$\left.\begin{aligned} a_{ij} &= \int_j (\ln r_{ij})' \, ds \\ b_{ij} &= -\int_j \ln r_{ij} \, ds \\ c_{ij} &= \int_j \rho_{ij}' \, ds \\ d_{ij} &= -\int_j \rho_{ij} \, ds \\ e_{ij} &= \int_j (\nabla^2 \rho_{ij})' \, ds \\ f_{ij} &= -\int_j \nabla^2 \rho_{ij} \, ds \end{aligned}\right\} \tag{11}$$

where integration is taken over the j^{th} interval, and r_{ij} is the distance from i^{th} node to any point in the j^{th} interval. The normal derivatives in equations (11) are taken on the j^{th} interval.

For curved boundaries the coefficients given by equations (11) can be evaluated, if necessary, by Simpson's rule for $i \neq j$. For $i = j$, because of the singular nature of the integrand, the integrals for the coefficients must be evaluated by a limiting process. For boundary intervals, such as for the problem treated herein, which can be represented by straight lines a closed form solution can be obtained for these coefficients.

Boundary equations (10) expressed in matrix form become

$$\begin{bmatrix} [a_{ij} - \delta_{ij}\pi]_{n\times n} & [b_{ij}]_{n\times n} \\ [c_{ij}]_{n\times n} & [d_{ij}]_{n\times n} \end{bmatrix} \begin{Bmatrix} [\Phi_j]_{n\times 1} \\ [\Phi'_j]_{n\times 1} \end{Bmatrix} = - \begin{bmatrix} [\ln r_{ik}]_{n\times m} & [0]_{n\times n} & [0]_{n\times n} \\ [\rho_{ik}]_{n\times m} & [e_{ij} - \delta_{ij}4\pi]_{n\times n} & [f_{ij}]_{n\times n} \end{bmatrix} \begin{Bmatrix} [(gA)_k]_{m\times 1} \\ [\varphi_j]_{n\times 1} \\ [\varphi'_j]_{n\times 1} \end{Bmatrix} \tag{12}$$

Thus, the problem is reduced to the solution of the following matrix system:

$$[B]\{X\} = \{R\} \tag{13}$$

where $[B]$ is $2n \times 2n$ matrix and $\{X\}$ and $\{R\}$ are $2n \times 1$ column matrices.

Matrix $[B]$ is dependent only on geometry, that is, number of nodes and their distribution on the boundary. Since the matrix $\{R\}$ contains the nonlinear function $g(\xi, \eta)$, which depends on the stress field and therefore on matrix $\{X\}$, an iterative process will be used to obtain the solution.

To calculate stresses, at any nodal point in the region R, from the stress function φ, we need not perform any numerical differentiation. Equation (5) can be differentiated under the integral sign and once Φ and Φ' are known on the boundary the stresses can be obtained by the same type of numerical integration as in equations (10). Applying equations (9) to equation (5) yields for the case of a rectangular grid the following stress equations:

$$
\left.
\begin{aligned}
8\pi\sigma_x(x, y)_i = &\left\{\left[\ln\left(\frac{\delta_x^2 + \delta_y^2}{4}\right) + \frac{2\delta_y}{\delta_x}\tan^{-1}\frac{\delta_x}{\delta_y} - 1\right](gA)\right\}_{i=k} \\
&+ \sum_{k=1}^{m}\left\{\ln\left[(x-\xi)^2 + (y-\eta)^2\right] + \frac{2(y-\eta)^2}{(x-\xi)^2 + (y-\eta)^2} + 1\right\}_{\substack{ik \\ i\neq k}} (gA)_k \\
&+ \sum_{j=1}^{n}\left(A_{ij}\varphi_j + B_{ij}\varphi_j' + C_{ij}\Phi_j + D_{ij}\Phi_j'\right) \\
8\pi\sigma_y(x, y)_i = &\left\{\left[\ln\left(\frac{\delta_x^2 + \delta_y^2}{4}\right) + \frac{2\delta_x}{\delta_y}\tan^{-1}\frac{\delta_y}{\delta_x} - 1\right](gA)\right\}_{i=k} \\
&+ \sum_{k=1}^{m}\left\{\ln\left[(x-\xi)^2 + (y-\eta)^2\right] + \frac{2(x-\xi)^2}{(x-\xi)^2 + (y-\eta)^2} + 1\right\}_{\substack{ik \\ i\neq k}} (gA)_k \\
&+ \sum_{j=1}^{n}\left(-A_{ij}\varphi_j - B_{ij}\varphi_j' + E_{ij}\Phi_j + F_{ij}\Phi_j'\right) \\
-8\pi\sigma_{xy}(x, y)_i = &\sum_{k=1}^{m}\left[\frac{2(x-\xi)(y-\eta)}{(x-\xi)^2 + (y-\eta)^2}\right]_{\substack{ik \\ i\neq k}} (gA)_k + \sum_{j=1}^{n}\left(G_{ij}\varphi_j + H_{ij}\varphi_j' + I_{ij}\Phi_j + K_{ij}\Phi_j'\right)
\end{aligned}
\right\} \quad (14)
$$

where now $i = 1, 2, 3, \ldots, m$ and refers to the centroid of the i^{th} cell, δ_x and δ_y represent, respectively, x-directional and y-directional dimension of the cell. The coefficients A_{ij}, B_{ij}, C_{ij}, D_{ij}, E_{ij}, F_{ij}, G_{ij}, H_{ij}, I_{ij}, and K_{ij} are obtained by appropriate differentiation under the integral sign of the coefficients given by equations (11) and are listed in appendix A.

The stress function φ is not constant on the loaded boundaries BC and B'C'. The assumption that it is piece-wise constant may lead to appreciable errors in the numerical

results. To eliminate this source of error, the summations given in equations (10) and (14) for intervals lying on the loaded boundaries and involving the stress function are replaced by direct integration.

Boundary Interval and Interior Grid Size

The number of nodal points prescribed for the boundary is theoretically unlimited. However, computer storage capacity for the computer used and difficulties associated with inversion of large matrices limited the order of the coefficient matrix [B] of equation (13) used herein to 140.

Because of geometric and loading symmetry about the x-axis, it is possible to reduce the number of unknowns. For 2n total number of nodal points the number of equations and unknowns, Φ_i and Φ_i', is reduced from 4n to 2n. Additional reduction in the number of unknowns is accomplished by taking into consideration St. Venant's effect at the loaded boundaries (ref. 2).

Since the vicinity of the crack tip is of greatest interest, a fine nodal spacing along the notch was chosen. To reduce the error introduced by the change in the interval size (ref. 10) around boundary points A and A' and at the same time to obtain fine resolution at the tip of the notch, the boundary along the notch was divided into a number of intervals progressively decreasing in length. The rate of change in the interval length and the resulting length of the smallest interval was found to have a great influence on the stress field in the vicinity of the tip of the notch. The rate of change in the interval's length along these boundaries was optimized by the method presented in reference 5. For the cases considered optimum ratios of the lengths of two consecutive boundary intervals were found to be in the range of 1.08 to 1.10. The resulting smallest dimensionless boundary interval length varied from 0.0001 to 0.0002. The nodal arrangement shown in figure 5 was used for all cases considered, resulting in a set of 140 equations containing 140 unknowns. Note that the corner points are always designated as interval points, never as nodal points, thus eliminating discontinuous functions from numerical analysis.

The choice of the size of the grid, which has to cover the region where plastic flow is expected to occur, is of utmost importance. A too coarse grid will not detect changes in the values of plastic-strain for small loading increments. A too fine mesh size may result in distorted values of second-order derivatives of plastic strains, which appear in the function g(x, y). The loading increment and the grid size are related to each other. A bad choice of either of them could result in the divergence of the iterative process. To allow the maximum of grid points to be within the expected plastic zone, a variable grid spacing was chosen. The grid used for plane strain conditions was finer, in general, than the one used for plane stress case.

The interior region, where plastic flow is expected, was divided into $r \times s$ rectangular cells. Due to symmetry about the x-axis, the number of unknown functions g, appearing in the boundary equations (10) and stress equations (14), was reduced from $r \times s$ to $m = r \times (s + 1)/2$, where now the coefficients of these functions represent the sum of the effect of left-hand and right-hand sides of the plastic field. Because of computation time limitations, the grid was arranged in 27×23 cell pattern, resulting in the number of unknowns g to be equal to 324. By increasing the number of unknowns to 400, the computation time for one iteration almost doubled. The smallest cells, located in the vicinity of the tip of the notch, have dimensions $\delta_x/w = 0.004$; $\delta_y/w = 0.008$ for plane strain cases, and $\delta_x/w = 0.004$, $\delta_y/w = 0.016$ for plane stress cases.

Cells with centroids outside the boundary of the beam above the tip of the notch were discarded and corresponding values of g were set equal to zero. A typical interior grid is shown in figure 5.

Central difference equations, given in appendix B, were used to evaluate $g(x, y)$ only for interior plastic cells, that is, where there was plastic flow at all eight adjacent cells. For noninterior cells the function was taken as an average of values of g at neighboring plastic cells. Other methods of dealing with g at centroids of noninterior plastic cells, such as backward differences of extrapolation, led to oscillation or divergences of the iterative process.

Method of Successive Elastic Solutions

The solution to this boundary value problem is obtained by an iterative process, known as the method of successive elastic solutions described in detail in reference 8. This method, applied to the present problem, proceeds as follows. The loading path is divided into a number of sufficiently small increments $\Delta\sigma_{max, i}$. The g function in the inhomogeneous equation (1) is thought of as a sum of Δg_i functions, each corresponding to its load increment $\Delta\sigma_{max, i}$. Each Δg_i is defined in terms of derivatives of the current plastic strain increments, $\Delta\epsilon_x^p$, $\Delta\epsilon_y^p$, and $\Delta\epsilon_{xy}^p$, which in turn depend, through equivalent plastic strain increment $\Delta\epsilon_p$, on the equivalent stress $\sigma_{e, i-1}$ associated with the previous load. The current plastic strain increments change iteratively as changing Δg_i affects the stress field.

The iterative procedure for determining plastic strain increments for each load increment is as follows:

(1) Select a value of load $\sigma_{max, i}$.

(2) Guess initial values of plastic strain increments. For the first load increment, assume all values to be equal to zero. Otherwise, use the converged values from the previous load increment.

(3) Calculate $g_i = g_{i-1} + \Delta g_i$.

(4) Calculate Φ_i and Φ_i' from boundary equations (10).

(5) Calculate the stresses from stress equations (14).

(6) Calculate modified total strains ϵ'_{ij} and the equivalent modified total strain ϵ_{et} from the following equations:

$$\epsilon'_{ij} = \epsilon^e_{ij} + \Delta\epsilon^p_{ij} \tag{15}$$

$$\epsilon_{et} = \frac{\sqrt{2}}{3}\sqrt{(\epsilon'_x - \epsilon'_y)^2 + (\epsilon'_x - \epsilon'_z)^2 + (\epsilon'_y - \epsilon'_z)^2 + 6\epsilon'^2_{xy}} \tag{16}$$

where ϵ^e_{ij} are the elastic strains computed from the stresses obtained in step (5).

(7) Calculate the equivalent plastic strain increment from

$$\Delta\epsilon_p = \frac{\epsilon_{et} - \frac{2}{3}\frac{1+\mu}{E}\sigma_{e,i-1}}{1 + \frac{2}{3}\frac{1+\mu}{E}\left(\frac{d\sigma_e}{d\epsilon_p}\right)_{i-1}} \tag{17}$$

with

$$\sigma_e = \frac{1}{\sqrt{2}}\sqrt{(\sigma_x - \sigma_y)^2 + (\sigma_y - \sigma_z)^2 + (\sigma_z - \sigma_x)^2 + 6\sigma^2_{xy}} \tag{18}$$

for plane strain case, and

$$\sigma_e = \sqrt{\sigma^2_x + \sigma^2_y - \sigma_x\sigma_y + 3\sigma^2_{xy}} \tag{19}$$

for plane stress case, where $\sigma_{e,i-1}$ is the value of the equivalent stress at the end of the previous increment of loading. For the first load increment and also for the case where there was no plastic flow under previous loading, $\sigma_{e,i-1}$ is equal to the yield stress σ_0. For the case of linear strain hardening equation (17) becomes

$$\Delta\epsilon_p = \frac{\epsilon_{et} - \frac{2}{3}\frac{1+\mu}{E}\sigma_{e,i-1}}{1 + \frac{2}{3}(1+\mu)\frac{m}{1-m}} \tag{20}$$

(8) Calculate a new set of plastic strain increments from

$$\left.\begin{aligned}
\Delta\epsilon_x^p &= \frac{\Delta\epsilon_p}{3\epsilon_{et}}\left(2\epsilon'_x - \epsilon'_y - \epsilon'_z\right) \\
\Delta\epsilon_y^p &= \frac{\Delta\epsilon_p}{3\epsilon_{et}}\left(2\epsilon'_y - \epsilon'_z - \epsilon'_x\right) \\
\Delta\epsilon_z^p &= \frac{\Delta\epsilon_p}{3\epsilon_{et}}\left(2\epsilon'_z - \epsilon'_x - \epsilon'_y\right) = -\left(\Delta\epsilon_x^p + \Delta\epsilon_y^p\right) \\
\Delta\epsilon_{xy}^p &= \frac{\Delta\epsilon_p}{\epsilon_{et}}\epsilon'_{xy}
\end{aligned}\right\} \tag{21}$$

(9) Repeat steps (3) to (8) until the plastic strain increments converge.

(10) Sum the plastic strain increments and return to step (1).

It should be noted at this point that the aforementioned procedure can be applied only where there is no unloading. Once the successive approximation procedure has converged, the stresses and strains are known everywhere in the beam.

The iterative process is illustrated by the flow diagram of figure 6.

Convergence

The convergence criterion is defined as an arbitrary maximum difference between successive values of one or more iterants. For the plastic field containing many points at which convergence is required, it is reasonable to set the convergence criterion based on an average value of the change in plastic strain increments. For the problems considered in this report, the convergence criterion was based on the convergence of plastic strain increments $\Delta\epsilon_y^p$ and was defined as

$$\frac{\dfrac{E}{\sigma_0}\displaystyle\sum_{j=1}^{n}\left|\Delta\epsilon^p_{y,k} - \Delta\epsilon^p_{y,k-1}\right|_j}{n} < T \tag{22}$$

where k refers to current iteration, n refers to number of plastic grid points for current iteration, and T is an arbitrary convergence parameter.

The computations were performed on a digital computer using a FORTRAN IV program with single-precision arithmetic. The matrix system given by equation (13) was solved using the modified Gauss elimination method, which utilizes pivoting and forward and backward substitutions.

The convergence parameter T was set to 0.003 or 0.005 depending on the load increment. Decreasing the convergence parameter T to 0.001 resulted in change in plastic strain increment values of approximately one in the third or fourth significant figure. For higher order accuracy, which does not appear to be necessary from a practical point of view, the computation time would be prohibitively long. The fact that the method of successive elastic solutions converges to the right answer has been shown by many examples in references 8 and 11.

RESULTS AND DISCUSSION

A number of beam problems were solved for both plane strain and plane stress cases. These included notch depth to beam depth ratios of 0.3 and 0.5, notch angles of 3° and 10°, strain hardening parameter values of 0.05 and 0.10. In addition, calculations were performed using the actual stress-strain curve of a 5083-0 aluminum alloy. For all cases Poisson's ratio was set at 0.33.

The load increment size used was necessarily a compromise between the accuracy desired and computational time required for convergence. For strain hardening parameter $m = 0.05$ the load increment size $\Delta\tilde{q}$ was taken equal to 0.05; while for $m = 0.10$, $\Delta\tilde{q} = 0.10$. For the case of a 5083-0 aluminum alloy, where the actual stress-strain curve (fig. 25) was used, the load was incremented by $\Delta\tilde{q} = 0.025$.

For the beam with dimensionless notch depth $\tilde{a} = 0.5$ the minimum load required to produce plastic flow at the most highly stressed grid points was found to be $\tilde{q} = 0.30$, and for $\tilde{a} = 0.3$ the initial load was found to be $\tilde{q} = 0.50$. The maximum load considered was $\tilde{q} = 0.7$ for the $\tilde{a} = 0.5$ cases, and $\tilde{q} = 0.9$ for the $\tilde{a} = 0.3$ cases. In the process of solving the aforementioned problems, the case with strain hardening parameter $m = 0.05$ required approximately 50 iterations for each increment of load (i.e., $\Delta\tilde{q} = 0.05$) for the relatively fine convergence parameter used. For cases where the strain hardening parameter $m = 0.10$ the average number of iterations needed for each increment of load (i.e., $\Delta\tilde{q} = 0.10$) was reduced to 40, while use of the actual stress-strain curve resulted in convergence in approximately 10 iterations for the plane strain case and in 20 iterations for the plane stress case.

Typical results of the computations are presented in figures 7 to 27 and tables I and II. Complete detailed results are given in reference 9.

The growth of the plastic zone with load is shown in figures 7 to 14. It is seen that the shapes of the elastoplastic boundaries remain similar to each other as the load in-

creases. As expected, plastic flow starts around the tip of the notch and as the load increases appears also at the boundary opposite the notch. Comparison of figures 11 and 12 with figures 13 and 14 shows that for the same loads the size of the plastic zones for plane strain are considerably smaller than for plane stress.

The equivalent stress contours in the vicinity of the notch for maximum applied loads are plotted for two cases in figures 15 and 16. The curves are the loci of all points of constant equivalent stress. The curves corresponding to $\sigma_e/\sigma_0 = 1$ indicate the boundary of the plastic zone. In addition, an elastic yield locus representing the elastoplastic boundary based on the elastic solution is shown in each case. Since this is commonly assumed to be the boundary of the plastic zone, we can see that for plane strain cases this assumption introduces considerable error along the x-axis. Along this axis the lengths of plastic zones obtained by elastoplastic and elastic solutions vary by a factor of about two.

Stresses and strains were calculated in all cases for interior grid points. Typical results of these calculations are given in figures 17 to 22.

The order of the stress singularity n was determined for each case by the method described in reference 5. The results are given in tables I and II. In case of plane strain conditions, the stress singularity decreases slowly as loading increases. In the case of the plane stress condition we have a sudden drop in n from its elastic value as plastic flow appears. Subsequently n slowly increases approaching a limit as the load increases.

The product of y-directional stress and total strain was calculated for various cases. The order of singularity of that product was determined by plotting $\ln(\sigma_y \epsilon_y)$ against $\ln r$ and by making a least squares fit of a straight line through the plotted points. It was found to be very close to unity for all cases considered.

In the case of an elastoplastic problem the stress intensity factor K_I defined in reference 2, must be generalized to the form

$$K_I^*(\sigma_{max}) = \lim_{r \to 0} \sqrt{2\pi}\, r^{n(\sigma_{max})} \sigma_y(r, \theta)\Big|_{\theta=0} \tag{23}$$

For linear elastic behavior K_I^* is identical with K_I.

Variation of the dimensionless generalized stress intensity factor with load is shown in figure 23 for the case of a specimen with notch depth of $\tilde{a} = 0.5$ and $\alpha = 10^o$, under plane strain condition and two values of strain hardening parameter m. The stress intensity factor shows no significant increase over the linear elastic value up to an applied load of $\tilde{q} = 0.40$. Above this load $\tilde{K}_I^*$ increases progressively for both m's, at the faster rate for lower strain hardening parameter.

The y-directional notch opening displacement was obtained for each case by numerical integration of the relation $\epsilon_{ij} = (1/2)(u_{i,j} + u_{j,i})$ along straight line paths. For each case a number of paths were chosen through the plastic region near the notch, and the resulting displacements were averaged. In general, the notch opening displacement varies linearly with the load until the plastic zone is established at the boundary opposite the notch. Then it increases rapidly, reaching values several times that which would be calculated from the elastic solution.

In order to verify in part the accuracy of the method used, a comparison of notch opening displacements was made with experimental results obtained by Bubsey and Jones (private communication from R. T. Bubsey and M. H. Jones of NASA Lewis Research Center). The specimen used in this experiment, made of aluminum 5083-0 with a length to width ratio of 4 and a crack length $\tilde{a} = 0.5$, was subjected to three-point bending. The stress-strain curve for this specimen is shown in figure 25. The experimental results as shown in figure 24 are in good agreement with numerical results obtained herein.

Finally, the J integral was evaluated for several cases by using relations given in reference 5. As in notch opening displacement calculations, straight line paths were chosen through the plastic zone near the tip of the notch. The integral was evaluated using values of stresses, strains, and displacements at cell centroids for a number of paths. The path independence of J was not conclusive, since the results varied up to 15 percent from the averaged value. It is possible that the results obtained herein do not indicate that the path independent property is lost but rather that the field values of the displacements are not calculated with sufficient accuracy.

The average values of the dimensionless $\tilde{J}$ integral as a function of load are plotted in figure 26 for a case of a specimen with a 10^{o} edge notch, $\tilde{a} = 0.5$, $m = 0.05$, and plane strain condition. At the start of plastic flow $\tilde{J}$ increases rapidly with load. This is followed by almost linear variation with additional load.

The relations between the J integral and stress intensity factor K_I developed for linear elasticity are obviously not applicable for the elastoplastic problem. By plotting the $\tilde{J}/\tilde{K}_I^{*2}$ ratios as a function of load $\tilde{q}$, the relation between the $\tilde{J}$ integral and the dimensionless generalized stress intensity factor $\tilde{K}_I^*$ is obtained. Typical plots are shown in figure 27. In all cases, the ratio $\tilde{J}/\tilde{K}_I^{*2}$ remains almost equal to elastic value of 0.89 for plane strain or 1.0 for plane stress and increases sharply at the load corresponding to the appearance of the plastic zone at the boundary opposite the notch. Once the transition occurs the ratio increases approximately proportionally to the load increment.

CONCLUSIONS

The boundary integral equation method proved to be capable of giving very detailed results such as stress and strain distributions around the tip of the notch and, related to them, the shapes of plastic zones. This was accomplished using a relatively small number of unknowns.

The obtained results also provide the information on the effect of strain hardening and on the differences that occur between plane stress and plane strain solutions. The singular nature of stresses and strains in the vicinity of the tip of the notch was confirmed. The order of singularity for the strain energy density was found to be unity, which is consistent with results previously obtained by other investigators.

The generalized stress intensity factor was introduced and calculated for several cases. The path independence property of the J integral was qualitatively confirmed and the relation between J and the generalized stress intensity factor was graphically extended to materials deforming according to the Prandtl-Reuss theory of plasticity.

The presence of a singularity at the tip of the notch makes accurate answers very difficult to obtain. Nevertheless good agreement was obtained between the calculated results and experimentally measured notch opening displacement as shown in figure 24. Some improvement in the solution techniques and further investigation of the influence of the boundary nodal spacing and interior grid size on the resulting stress and strain fields, and therefore, on the notch opening displacements and J integrals, may be desirable.

Lewis Research Center,
National Aeronautics and Space Administration,
Cleveland, Ohio, January 7, 1974,
501-21.

APPENDIX A

COEFFICIENTS OF THE STRESS EQUATIONS

The coefficients appearing in stress equations (14) are given by the following relations:

$$A_{ij} = \frac{\partial^2}{\partial y^2}(e_{ij}) = 4\int_j \frac{\partial}{\partial n}\left\{\frac{(x_i - \xi)^2 - (y_i - \eta)^2}{\left[(x_i - \xi)^2 + (y_i - \eta)^2\right]^2}\right\} ds$$

$$B_{ij} = \frac{\partial^2}{\partial y^2}(f_{ij}) = 4\int_j \frac{(y_i - \eta)^2 - (x_i - \xi)^2}{\left[(x_i - \xi)^2 + (y_i - \eta)^2\right]^2} ds$$

$$C_{ij} = \frac{\partial^2}{\partial y^2}(c_{ij}) = \int_j \frac{\partial}{\partial n}\left\{\ln\left[(x_i - \xi)^2 + (y_i - \eta)^2\right] + \frac{2(y_i - \eta)^2}{(x_i - \xi)^2 + (y_i - \eta)^2}\right\} ds$$

$$D_{ij} = \frac{\partial^2}{\partial y^2}(d_{ij}) = -\int_j \left\{\ln\left[(x_i - \xi)^2 + (y_i - \eta)^2\right] + \frac{2(y_i - \eta)^2}{(x_i - \xi)^2 + (y_i - \eta)^2} + 1\right\} ds$$

$$E_{ij} = \frac{\partial^2}{\partial x^2}(c_{ij}) = \int_j \frac{\partial}{\partial n}\left\{\ln\left[(x_i - \xi)^2 + (y_i - \eta)^2\right] + \frac{2(x_i - \xi)^2}{(x_i - \xi)^2 + (y_i - \eta)^2}\right\} ds$$

$$F_{ij} = \frac{\partial^2}{\partial x^2}(d_{ij}) = -\int_j \left\{\ln\left[(x_i - \xi)^2 + (y_i - \eta)^2\right] + \frac{2(x_i - \xi)^2}{(x_i - \xi)^2 + (y_i - \eta)^2} + 1\right\} ds$$

$$G_{ij} = \frac{\partial^2}{\partial x\, \partial y}(e_{ij}) = -8 \int_j \frac{\partial}{\partial n}\left\{\frac{(x_i - \xi)(y_i - \eta)}{\left[(x_i - \xi)^2 + (y_i - \eta)^2\right]^2}\right\} ds$$

$$H_{ij} = \frac{\partial^2}{\partial x\, \partial y}(f_{ij}) = 8 \int_j \frac{(x_i - \xi)(y_i - \eta)}{\left[(x_i - \xi)^2 + (y_i - \eta)^2\right]^2} ds$$

$$I_{ij} = \frac{\partial^2}{\partial x\, \partial y}(c_{ij}) = 2 \int_j \frac{\partial}{\partial n}\left[\frac{(x_i - \xi)(y_i - \eta)}{(x_i - \xi)^2 + (y_i - \eta)^2}\right] ds$$

$$K_{ij} = \frac{\partial^2}{\partial x\, \partial y}(d_{ij}) = -2 \int_j \frac{(x_i - \xi)(y_i - \eta)}{(x_i - \xi)^2 + (y_i - \eta)^2} ds$$

The evaluation of these integrals is given in reference 9.

APPENDIX B

NUMERICAL REPRESENTATION OF THE FUNCTION OF PLASTIC STRAINS g(x, y)

Before we can proceed with the numerical solution, it is necessary to represent the function of plastic strains g(x, y), given by equation (2) or (3), by corresponding finite-difference equations.

The finite-difference net for grid station (r, s) is shown in figure 28. For a given function f = f(x, y), by use of central differences, we can obtain the following expressions for derivatives of this function:

$$
\left.
\begin{aligned}
f_x &= \beta_{r-1,s}(f_{r-1,s} - f_{r,s}) + \beta_{r+1,s}(f_{r+1,s} - f_{r,s}) \\
f_y &= \beta_{r,s-1}(f_{r,s-1} - f_{r,s}) + \beta_{r,s+1}(f_{r,s+1} - f_{r,s}) \\
f_{xx} &= \alpha_{r-1,s}(f_{r-1,s} - f_{r,s}) + \alpha_{r+1,s}(f_{r+1,s} - f_{r,s}) \\
f_{yy} &= \alpha_{r,s-1}(f_{r,s-1} - f_{r,s}) + \alpha_{r,s+1}(f_{r,s+1} - f_{r,s}) \\
f_{xy} &= \gamma_{r-1,s-1}f_{r-1,s-1} + \gamma_{r-1,s}f_{r-1,s} + \gamma_{r-1,s+1}f_{r-1,s+1} \\
&\quad + \gamma_{r,s-1}f_{r,s-1} + \gamma_{r,s}f_{r,s} + \gamma_{r,s+1}f_{r,s+1} + \gamma_{r+1,s-1}f_{r+1,s-1} \\
&\quad + \gamma_{r+1,s}f_{r+1,s} + \gamma_{r+1,s+1}f_{r+1,s+1}
\end{aligned}
\right\} \quad \text{(B1)}
$$

where subscripts x, y denote differentiation with respect to variable x or y, r is a row index, s is a column index, and the coefficients are given by the following relations:

$$\alpha_{r-1,\,s} = \frac{2}{\Delta x\,\Delta x_T}$$

$$\alpha_{r+1,\,s} = \frac{2}{\Delta x\,\Delta x_B}$$

$$\alpha_{r,\,s-1} = \frac{2}{\Delta y\,\Delta y_L}$$

$$\alpha_{r,\,s+1} = \frac{2}{\Delta y\,\Delta y_R}$$

$$\beta_{r-1,\,s} = -\frac{\Delta x_B}{\Delta x\,\Delta x_T}$$

$$\beta_{r+1,\,s} = \frac{\Delta x_T}{\Delta x\,\Delta x_B}$$

$$\beta_{r,\,s-1} = -\frac{\Delta y_R}{\Delta y\,\Delta y_L}$$

$$\beta_{r,\,s+1} = \frac{\Delta y_L}{\Delta y\,\Delta y_R}$$

$$\gamma_{r-1,\,s-1} = \beta_{r-1,\,s}\beta_{r,\,s-1}$$

$$\gamma_{r-1,\,s+1} = \beta_{r-1,\,s}\beta_{r,\,s+1}$$

$$\gamma_{r+1,\,s-1} = \beta_{r,\,s-1}\beta_{r+1,\,s}$$

$$\gamma_{r+1,\,s+1} = \beta_{r,\,s+1}\beta_{r+1,\,s}$$

$$\gamma_{r-1,\,s} = -\gamma_{r-1,\,s-1} - \gamma_{r-1,\,s+1}$$

$$\gamma_{r,\,s-1} = -\gamma_{r-1,\,s-1} - \gamma_{r+1,\,s-1}$$

$$\gamma_{r,\,s+1} = -\gamma_{r-1,\,s+1} - \gamma_{r+1,\,s+1}$$

$$\gamma_{r+1,\,s} = -\gamma_{r+1,\,s-1} - \gamma_{r+1,\,s+1}$$

$$\gamma_{r,\,s} = \gamma_{r-1,\,s-1} + \gamma_{r-1,\,s+1} + \gamma_{r+1,\,s-1} + \gamma_{r+1,\,s+1}$$

(B2)

where Δx, Δy, Δx_T, Δx_B, Δy_L, and Δy_R are distances as defined in figure 28. When relations (B1) and (B2) are used, the function $g(x, y)$ can be expressed by following finite-difference expressions:

$$
\begin{aligned}
g(x, y) = \frac{\mu E}{1 - \mu^2} \Bigg[& \alpha_{r-1, s}\left(\epsilon_x^p + \Delta\epsilon_x^p\right)_{r-1, s} - (\alpha_{r-1, s} + \alpha_{r+1, s})\left(\epsilon_x^p + \Delta\epsilon_x^p\right)_{r, s} \\
& + \alpha_{r+1, s}\left(\epsilon_x^p + \Delta\epsilon_x^p\right)_{r+1, s} + \alpha_{r, s-1}\left(\epsilon_y^p + \Delta\epsilon_y^p\right)_{r, s-1} \\
& - (\alpha_{r, s-1} + \alpha_{r, s+1})\left(\epsilon_y^p + \Delta\epsilon_y^p\right)_{r, s} + \alpha_{r, s+1}\left(\epsilon_y^p + \Delta\epsilon_y^p\right)_{r, s+1} \Bigg] \\
& - \frac{E}{1 + \mu} \Bigg[\alpha_{r, s-1}\left(\epsilon_x^p + \Delta\epsilon_x^p\right)_{r, s-1} - (\alpha_{r, s-1} + \alpha_{r, s+1})\left(\epsilon_x^p + \Delta\epsilon_x^p\right)_{r, s} \\
& + \alpha_{r, s+1}\left(\epsilon_x^p + \Delta\epsilon_x^p\right)_{r, s+1} + \alpha_{r-1, s}\left(\epsilon_y^p + \Delta\epsilon_y^p\right)_{r-1, s} \\
& - (\alpha_{r-1, s} + \alpha_{r+1, s})\left(\epsilon_y^p + \Delta\epsilon_y^p\right)_{r, s} + \alpha_{r+1, s}\left(\epsilon_y^p + \Delta\epsilon_y^p\right)_{r+1, s} \Bigg] \\
& + \frac{2E}{1 - \mu^2} \Bigg[\gamma_{r-1, s-1}\left(\epsilon_{xy}^p + \Delta\epsilon_{xy}^p\right)_{r-1, s-1} + \gamma_{r-1, s}\left(\epsilon_{xy}^p + \Delta\epsilon_{xy}^p\right)_{r-1, s} \\
& + \gamma_{r-1, s+1}\left(\epsilon_{xy}^p + \Delta\epsilon_{xy}^p\right)_{r-1, s+1} + \gamma_{r, s-1}\left(\epsilon_{xy}^p + \Delta\epsilon_{xy}^p\right)_{r, s-1} \\
& + \gamma_{r, s}\left(\epsilon_{xy}^p + \Delta\epsilon_{xy}^p\right)_{r, s} + \gamma_{r, s+1}\left(\epsilon_{xy}^p + \Delta\epsilon_{xy}^p\right)_{r, s+1} \\
& + \gamma_{r+1, s-1}\left(\epsilon_{xy}^p + \Delta\epsilon_{xy}^p\right)_{r+1, s-1} + \gamma_{r+1, s}\left(\epsilon_{xy}^p + \Delta\epsilon_{xy}^p\right)_{r+1, s} \\
& + \gamma_{r+1, s+1}\left(\epsilon_{xy}^p + \Delta\epsilon_{xy}^p\right)_{r+1, s+1} \Bigg] \qquad \text{Plane strain}
\end{aligned}
\tag{B3}
$$

$$
\begin{aligned}
g(x, y) = -E \Big\{ & \alpha_{r, s-1}\left(\epsilon_x^p + \Delta\epsilon_x^p\right)_{r, s-1} - (\alpha_{r, s-1} + \alpha_{r, s+1})\left(\epsilon_x^p + \Delta\epsilon_x^p\right)_{r, s} \\
& + \alpha_{r, s+1}\left(\epsilon_x^p + \Delta\epsilon_x^p\right)_{r, s+1} + \alpha_{r-1, s}\left(\epsilon_y^p + \Delta\epsilon_y^p\right)_{r-1, s} \\
& - (\alpha_{r-1, s} + \alpha_{r+1, s})\left(\epsilon_y^p + \Delta\epsilon_y^p\right)_{r, s} + \alpha_{r+1, s}\left(\epsilon_y^p + \Delta\epsilon_y^p\right)_{r+1, s} \\
& - 2\Big[\gamma_{r-1, s-1}\left(\epsilon_{xy}^p + \Delta\epsilon_{xy}^p\right)_{r-1, s-1} + \gamma_{r-1, s}\left(\epsilon_{xy}^p + \Delta\epsilon_{xy}^p\right)_{r-1, s} \\
& + \gamma_{r-1, s+1}\left(\epsilon_{xy}^p + \Delta\epsilon_{xy}^p\right)_{r-1, s+1} + \gamma_{r, s-1}\left(\epsilon_{xy}^p + \Delta\epsilon_{xy}^p\right)_{r, s-1} \\
& + \gamma_{r, s}\left(\epsilon_{xy}^p + \Delta\epsilon_{xy}^p\right)_{r, s} + \gamma_{r, s+1}\left(\epsilon_{xy}^p + \Delta\epsilon_{xy}^p\right)_{r, s+1} \\
& + \gamma_{r+1, s-1}\left(\epsilon_{xy}^p + \Delta\epsilon_{xy}^p\right)_{r+1, s-1} + \gamma_{r+1, s}\left(\epsilon_{xy}^p + \Delta\epsilon_{xy}^p\right)_{r+1, s} \\
& + \gamma_{r+1, s+1}\left(\epsilon_{xy}^p + \Delta\epsilon_{xy}^p\right)_{r+1, s+1}\Big]\Big\} \qquad \text{Plane stress}
\end{aligned}
\tag{B4}
$$

REFERENCES

1. Bowie, O. L.: Rectangular Tensile Sheet with Symmetric Edge Cracks. J. Appl. Mech., vol. 86, no. 2, June 1964, pp. 208-212.

2. Gross, Bernard: Some Plane Problem Elastostatic Solutions for Plates Having a V-Notch. Ph.D. Thesis, Case Western Reserve Univ., 1970.

3. Hays, David James: Some Applications of Elastic-Plastic Analysis to Fracture Mechanics. Ph.D. Thesis, Imperial College of Science and Technology, Univ. London, 1970.

4. Mendelson, Alexander: Boundary Integral Methods in Elasticity and Plasticity. NASA TN D-7418, 1973.

5. Rzasnicki, Walter; Mendelson, Alexander; and Albers, Lynn U.: Application of Boundary Integral Method to Elastic Analysis of V-Notched Beams. NASA TN D-7424, 1973.

6. Swedlow, J. L.; and Cruse, T. A.: Formulation of Boundary Integral Equations for Three-Dimensional Elasto-Plastic Flow. Int. J. Solids Structures, vol. 7, no. 12, Dec. 1971, pp. 1673-1683.

7. Swedlow, J. L.; Williams, M. L.; and Yang, W. H.: Elasto-Plastic Stresses and Strains in Cracked Plates. Proceedings of the 1st International Conference on Fracture. Vol. 1. Takeo Yokobori, T. Kawasaki, and J. L. Swedlow, eds., Japanese Soc. Strength and Fracture of Materials, 1966, pp. 259-282.

8. Mendelson, Alexander: Plasticity: Theory and Application. Macmillan Co., 1968.

9. Rzasnicki, Walter: Plane Elasto-Plastic Analysis of V-Notched Plate Under Bending by Boundary Integral Equation Method. Ph.D. Thesis, Univ. Toledo, 1973.

10. Walker, George E., Jr.: A Study of the Applicability of the Method of Potential to Inclusions of Various Shapes in Two- and Three-Dimensional Elastic and Thermo-Elastic Stress Fields. Ph.D. Thesis, Univ. Washington, 1969.

11. Ilyushin, A. A.: Some Problems in the Theory of Plastic Deformations. Rep. BMB-12, Trans. by Grad. Div. Appl. Math., Brown Univ., for David W. Taylor Model Basin, 1946. (Contract NObs-34166.)

TABLE I. - ORDER OF STRESS SINGULARITY n AT THE TIP OF THE NOTCH FOR A SPECIMEN WITH A SINGLE EDGE NOTCH SUBJECTED TO PURE BENDING - PLANE STRAIN

[Poisson's ratio $\mu = 0.33$.]

Dimensionless notch depth, $\tilde{a}$	Notch angle, α, deg	Strain hardening parameter, m	Elastic	Dimensionless load, $\tilde{q}$					
				0.4	0.5	0.6	0.7	0.8	0.9
0.3	3	0.10	0.4999	-----	0.488	0.490	0.487	0.473	0.475
.3	10	.10	↓	-----	.496	.497	.492	.480	.487
.5	10	.05		0.499	.496	.480	.472	-----	-----
.5	10	.10		.496	.498	.480	.478	-----	-----

TABLE II. - ORDER OF STRESS SINGULARITY n AT THE TIP OF THE NOTCH FOR A SPECIMEN WITH A SINGLE EDGE NOTCH SUBJECTED TO PURE BENDING - PLANE STRESS

[Dimensionless notch depth $\tilde{a} = 0.3$; notch angle $\alpha = 10^{\circ}$; strain hardening parameter $m = 0.10$; Poisson's ratio $\mu = 0.33$.]

Elastic	Dimensionless load, $\tilde{q}$				
	0.5	0.6	0.7	0.8	0.9
0.4999	0.419	0.434	0.448	0.451	0.458

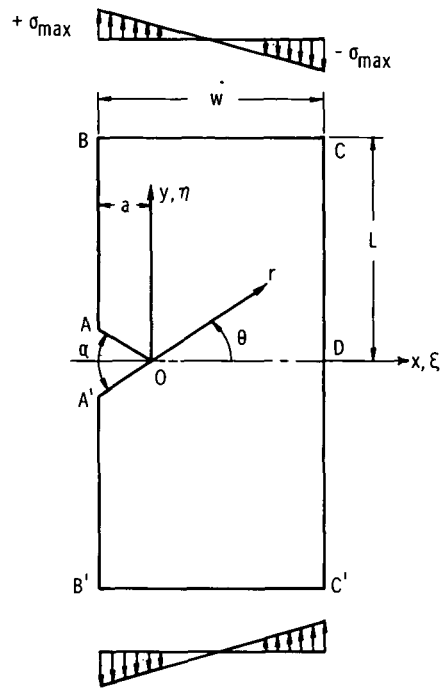

Figure 1. - Single-edge V-notched beam subject to pure bending load.

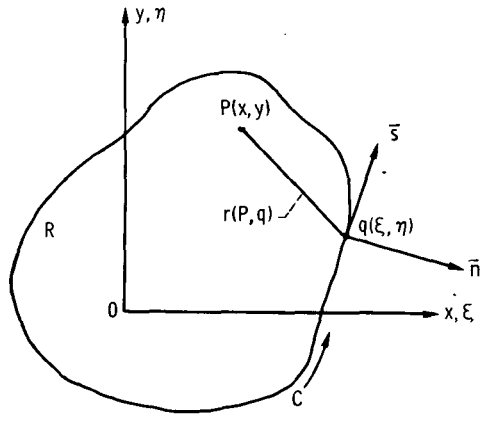

Figure 2. - Sign convention for simply connected region R.

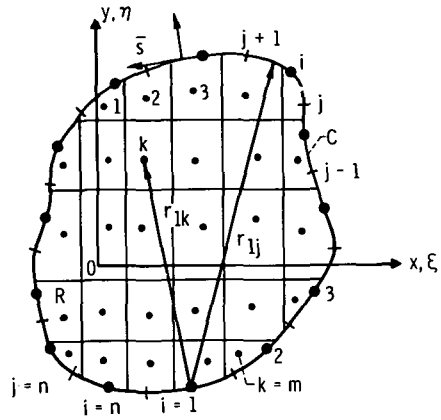

Figure 3. - Boundary and interior region subdivisions for P(x,y) ⊂ C.

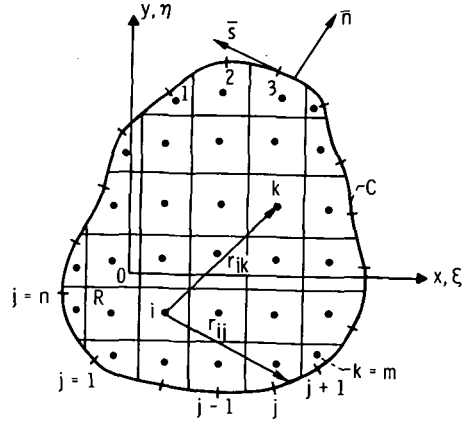

Figure 4. - Boundary and interior region subdivisions for P(x,y) ⊂ R.

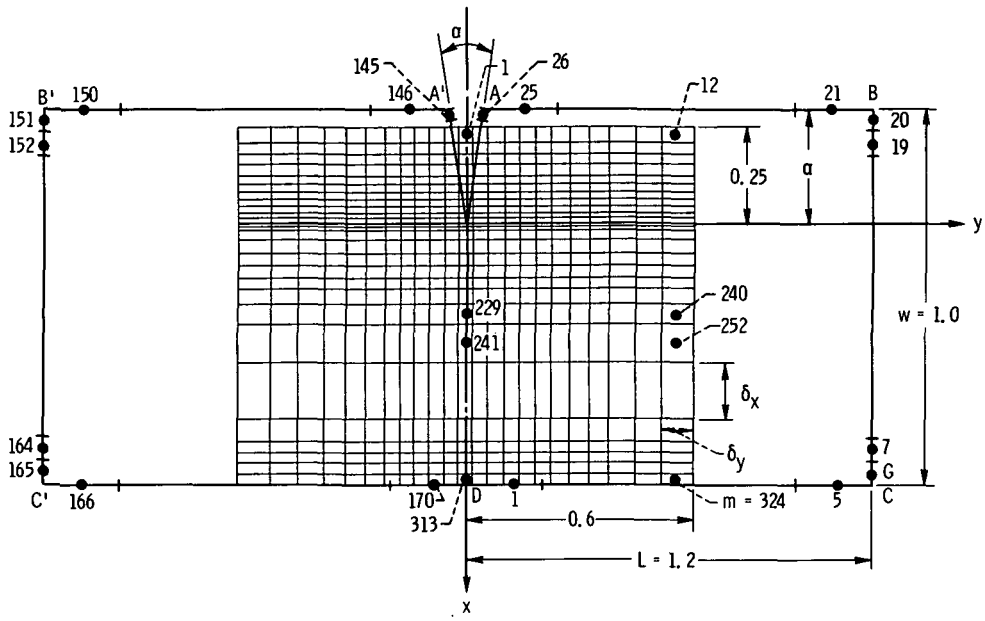

Figure 5. - Distribution of boundary subdivisions and typical interior grid for elastoplastic problem. (All distances are made dimensionless with respect to beam width w.)

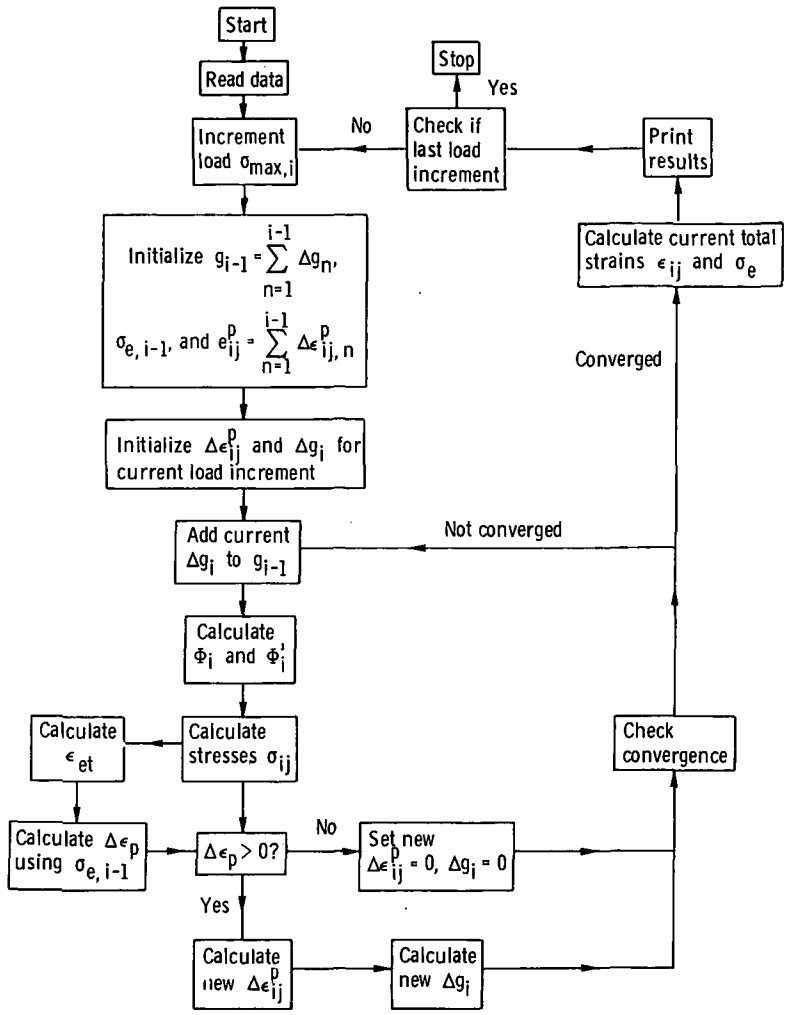

Figure 6. - Flow diagram for method of successive elastic solutions.

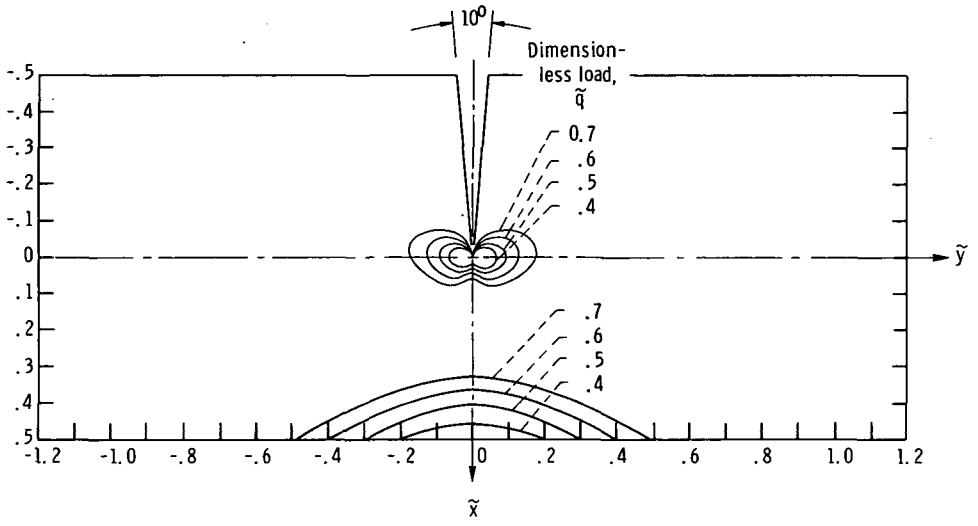

Figure 7. - Growth of plastic zone size with load for specimen with single edge notch subjected to pure bending. Plane strain; dimensionless notch depth $\tilde{a} = 0.5$; notch angle $\alpha = 10^{0}$; strain hardening parameter $m = 0.05$; Poisson's ratio $\mu = 0.33$.

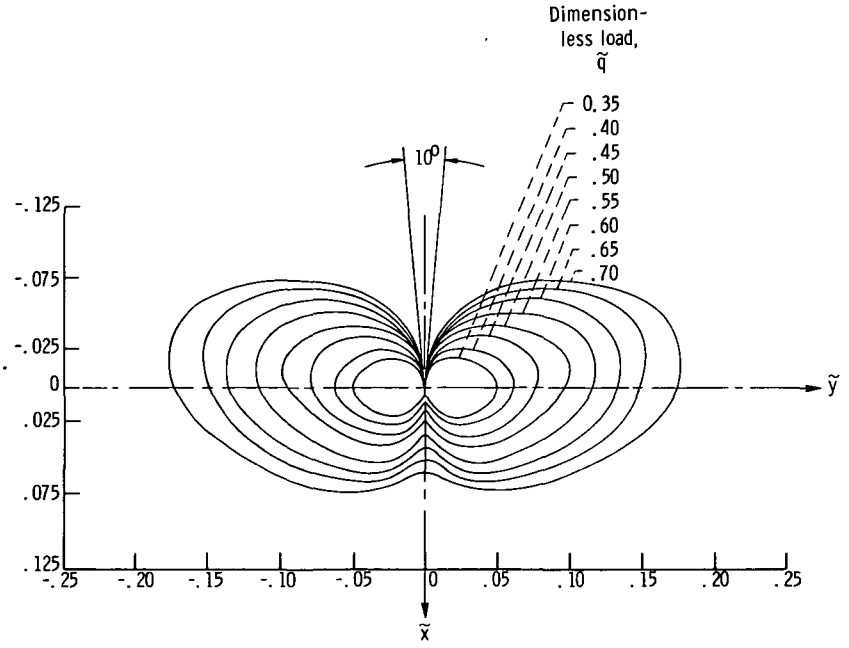

Figure 8. - Growth of plastic zone size with load in vicinity of notch for specimen with single edge notch subjected to pure bending. Plane strain; dimensionless notch depth $\tilde{a} = 0.5$; notch angle $\alpha = 10^{0}$; strain hardening parameter $m = 0.05$; Poisson's ratio $\mu = 0.33$.

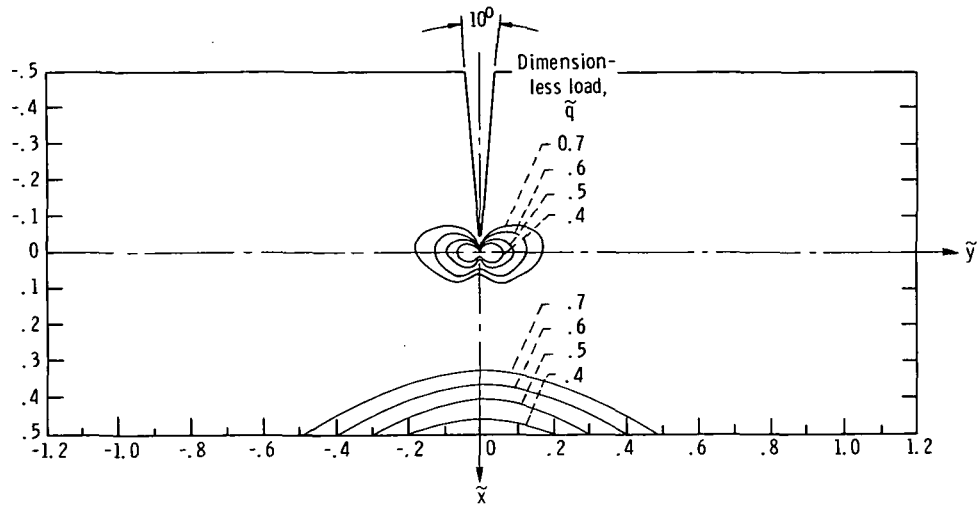

Figure 9. - Growth of plastic zone size with load for specimen with single edge notch subjected to pure bending. Plane strain; dimensionless notch depth $\tilde{a} = 0.5$; notch angle $\alpha = 10^0$; strain hardening parameter $m = 0.10$; Poisson's ratio $\mu = 0.33$.

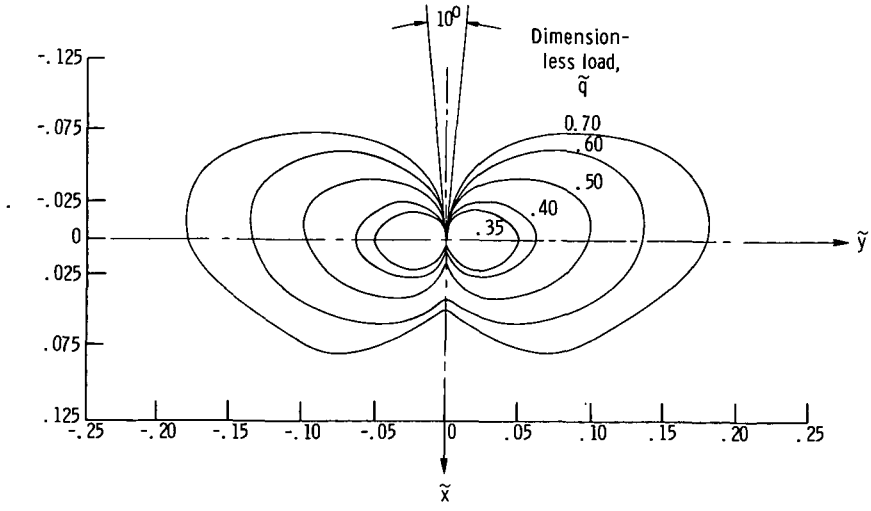

Figure 10. - Growth of plastic zone size with load in vicinity of notch for specimen with single edge notch subjected to pure bending. Plane strain; dimensionless notch depth $\tilde{a} = 0.5$; notch angle $\alpha = 10^0$; strain hardening parameter $m = 0.10$; Poisson's ratio $\mu = 0.33$.

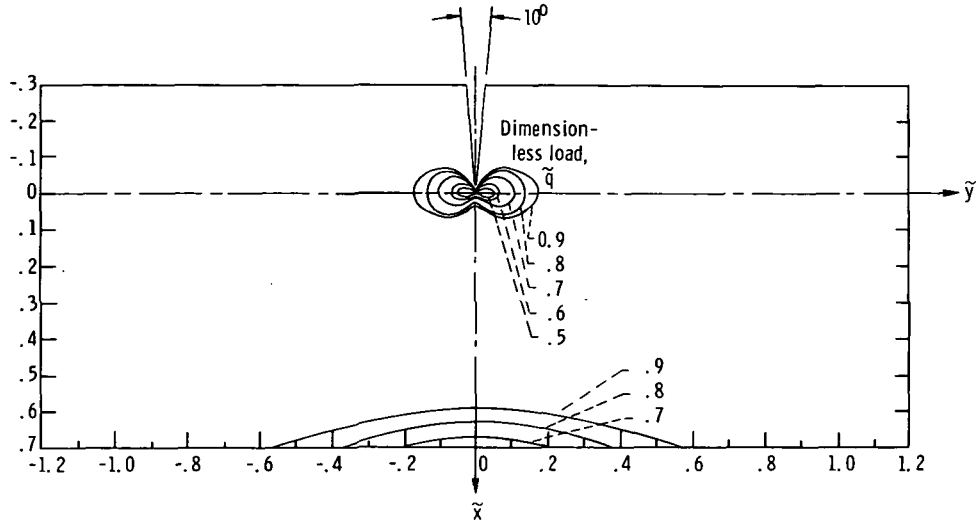

Figure 11. - Growth of plastic zone size with load for specimen with single edge notch subjected to pure bending. Plane strain; dimensionless notch depth $\tilde{a} = 0.3$; notch angle $\alpha = 10^{0}$; strain hardening parameter $m = 0.10$; Poisson's ratio $\mu = 0.33$.

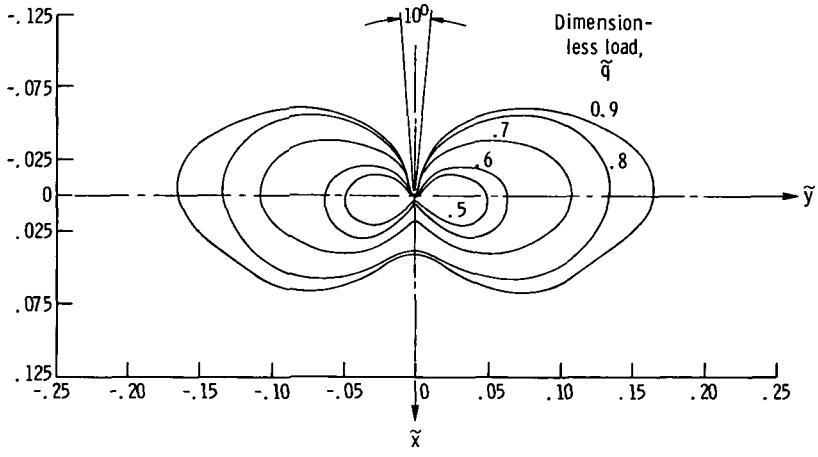

Figure 12. - Growth of plastic zone size with load in vicinity of notch for specimen with single edge notch subjected to pure bending. Plane strain; dimensionless notch depth $\tilde{a} = 0.3$; notch angle $\alpha = 10^{0}$; strain hardening parameter $m = 0.10$; Poisson's ratio $\mu = 0.33$.

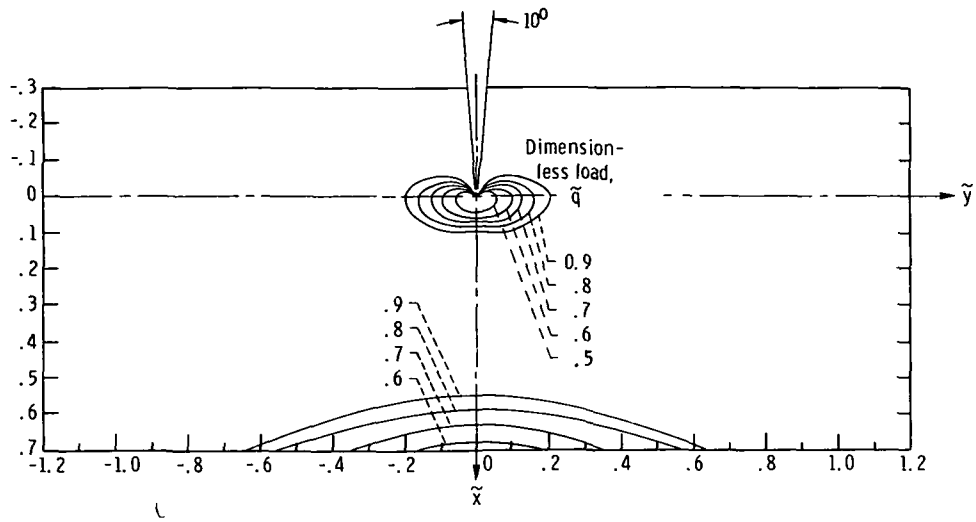

Figure 13. - Growth of plastic zone size with load for specimen with single edge notch subjected to pure bending. Plane stress; dimensionless notch depth $\tilde{a} = 0.3$; notch angle $\alpha = 10^0$; strain hardening parameter $m = 0.10$; Poisson's ratio $\mu = 0.33$.

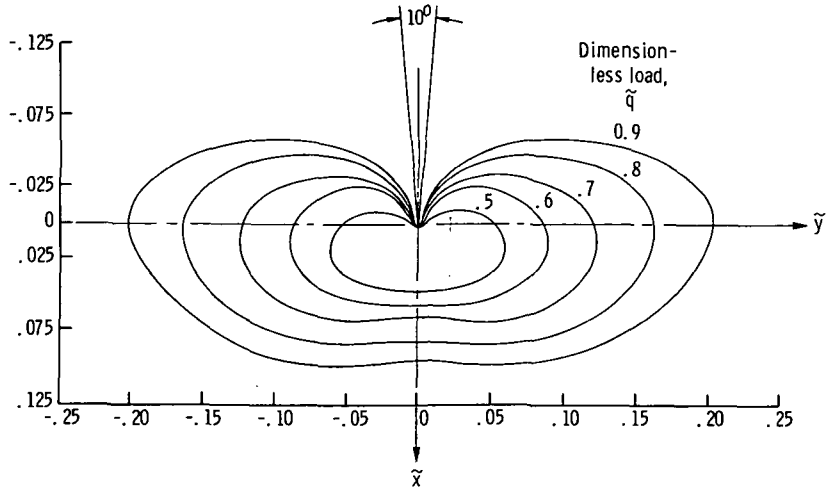

Figure 14. - Growth of plastic zone size with load in vicinity of notch for a specimen with single edge notch subjected to pure bending. Plane stress; dimensionless notch depth $\tilde{a} = 0.3$; notch angle $\alpha = 10^0$; strain hardening parameter $m = 0.10$; Poisson's ratio $\mu = 0.33$.

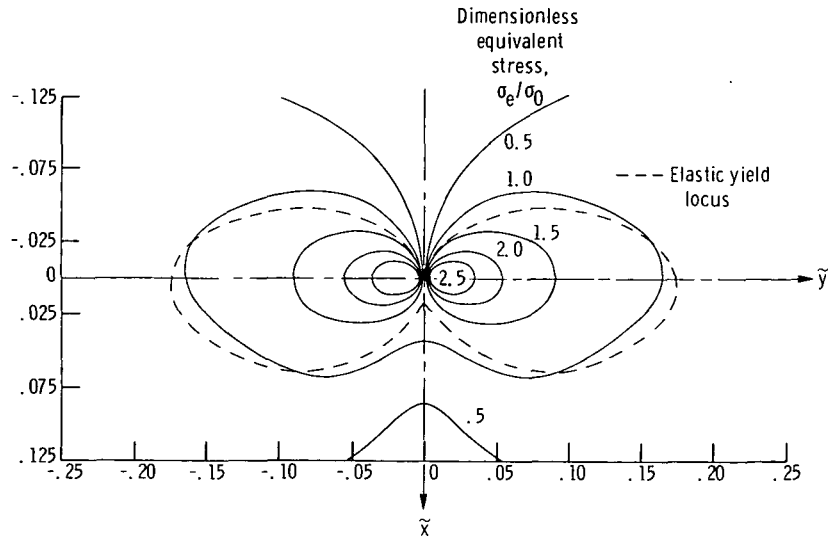

Figure 15. - Dimensionless equivalent stress contours in vicinity of notch for specimen with single edge notch subjected to pure bending. Plane strain; dimensionless load $\tilde{q} = 0.9$; dimensionless notch depth $\tilde{a} = 0.3$; notch angle $\alpha = 10^0$; strain hardening parameter $m = 0.10$; Poisson's ratio $\mu = 0.33$.

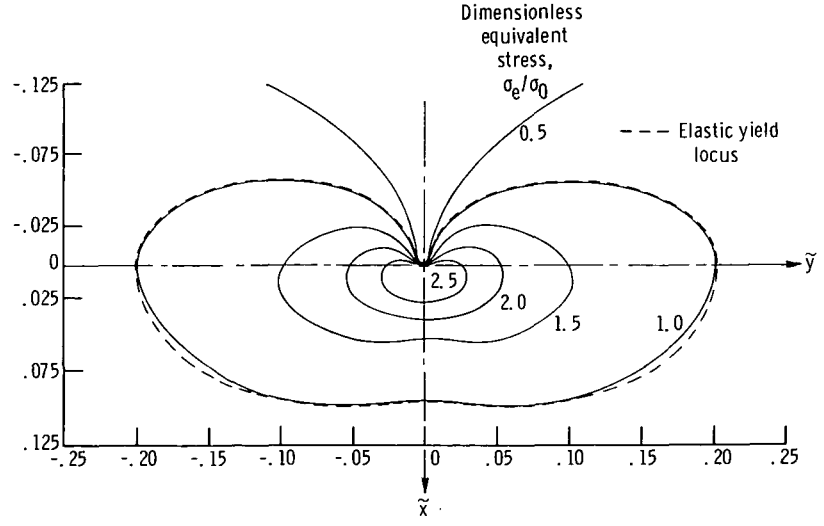

Figure 16. - Dimensionless equivalent stress contours in vicinity of notch for specimen with single edge notch subjected to pure bending. Plane stress; dimensionless load $\tilde{q} = 0.9$; dimensionless notch depth $\tilde{a} = 0.3$; notch angle $\alpha = 10^0$; strain hardening parameter $m = 0.10$; Poisson's ratio $\mu = 0.33$.

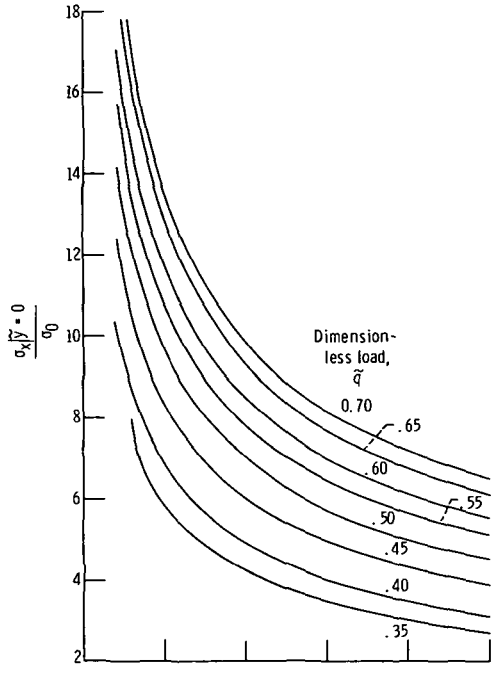

(a) Dimensionless x-directional stress as a function of $\tilde{x}$.

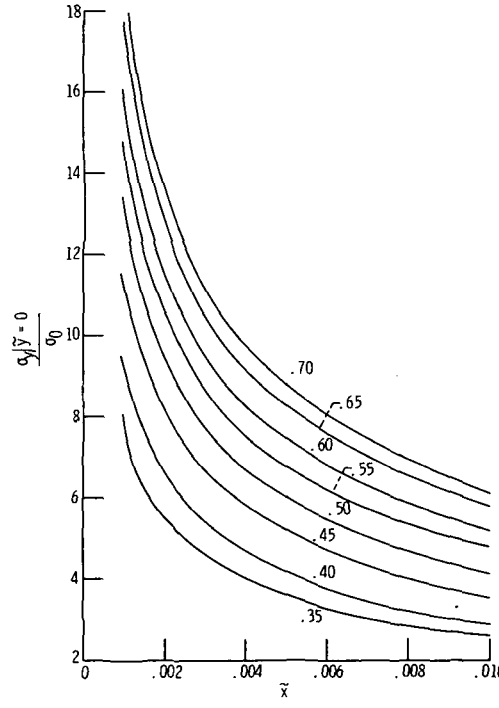

(b) Dimensionless y-directional stress as a function of $\tilde{x}$.

Figure 17. - Dimensionless x- and y-directional stress distribution in vicinity of notch for specimen with single edge notch subjected to pure bending. Plane strain; dimensionless notch depth $\tilde{a} = 0.5$; notch angle $\alpha = 10^0$; strain hardening parameter $m = 0.05$; Poisson's ratio $\mu = 0.33$.

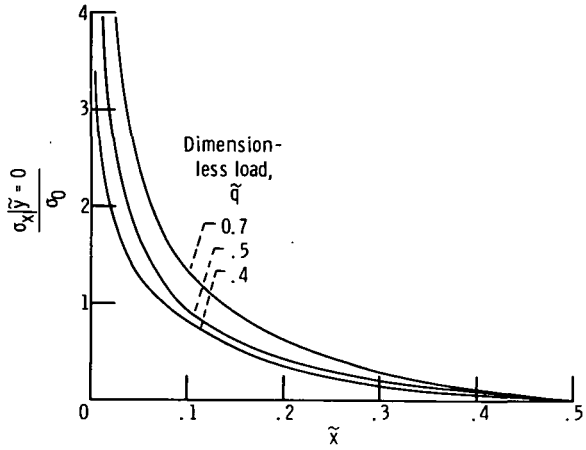

Figure 18. - Dimensionless x-directional stress distribution along x-axis for specimen with single edge notch subjected to pure bending. Plane strain; dimensionless notch depth $\tilde{a} = 0.5$; notch angle $\alpha = 10^0$; strain hardening parameter $m = 0.05$; Poisson's ratio $\mu = 0.33$.

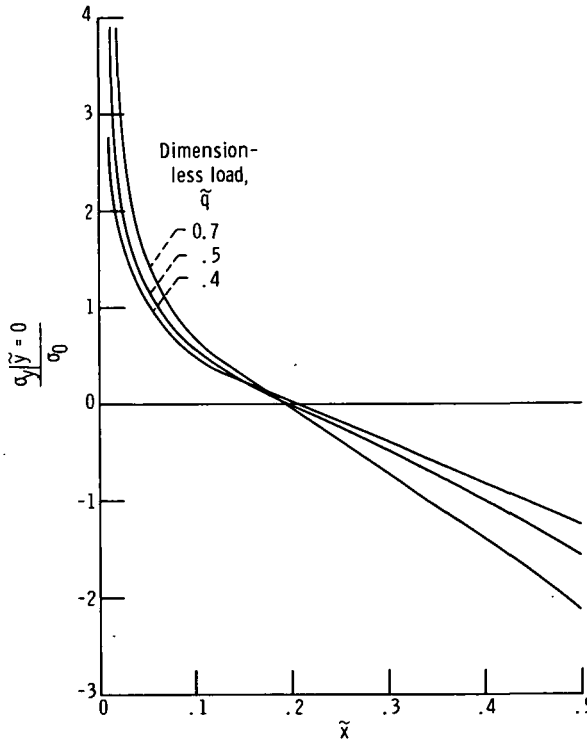

Figure 19. - Dimensionless y-directional stress distribution along x-axis for specimen with single edge notch subjected to pure bending. Plane strain; dimensionless notch depth $\tilde{a} = 0.5$; notch angle $\alpha = 10^0$; strain hardening parameter $m = 0.05$; Poisson's ratio $\mu = 0.33$.

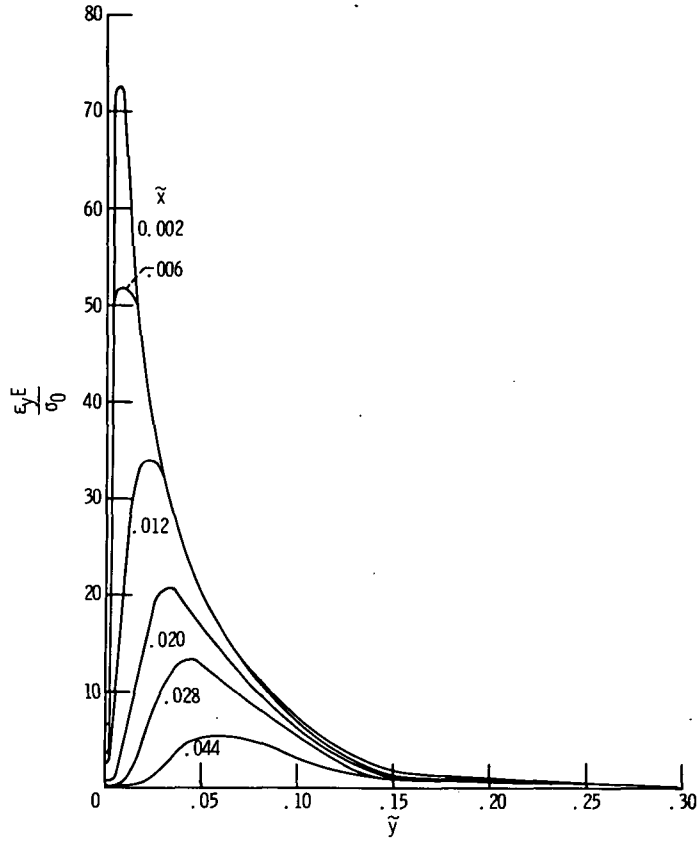

Figure 20. - Dimensionless y-directional total strain distribution along $\tilde{x}$ = constant lines in vicinity of notch for specimen with single edge notch subjected to pure bending. Plain strain; dimensionless load $\tilde{q}$ = 0.7; dimensionless notch depth $\tilde{a}$ = 0.5; notch angle $\alpha = 10^0$; strain hardening parameter m = 0.05; Poisson's ratio μ = 0.33.

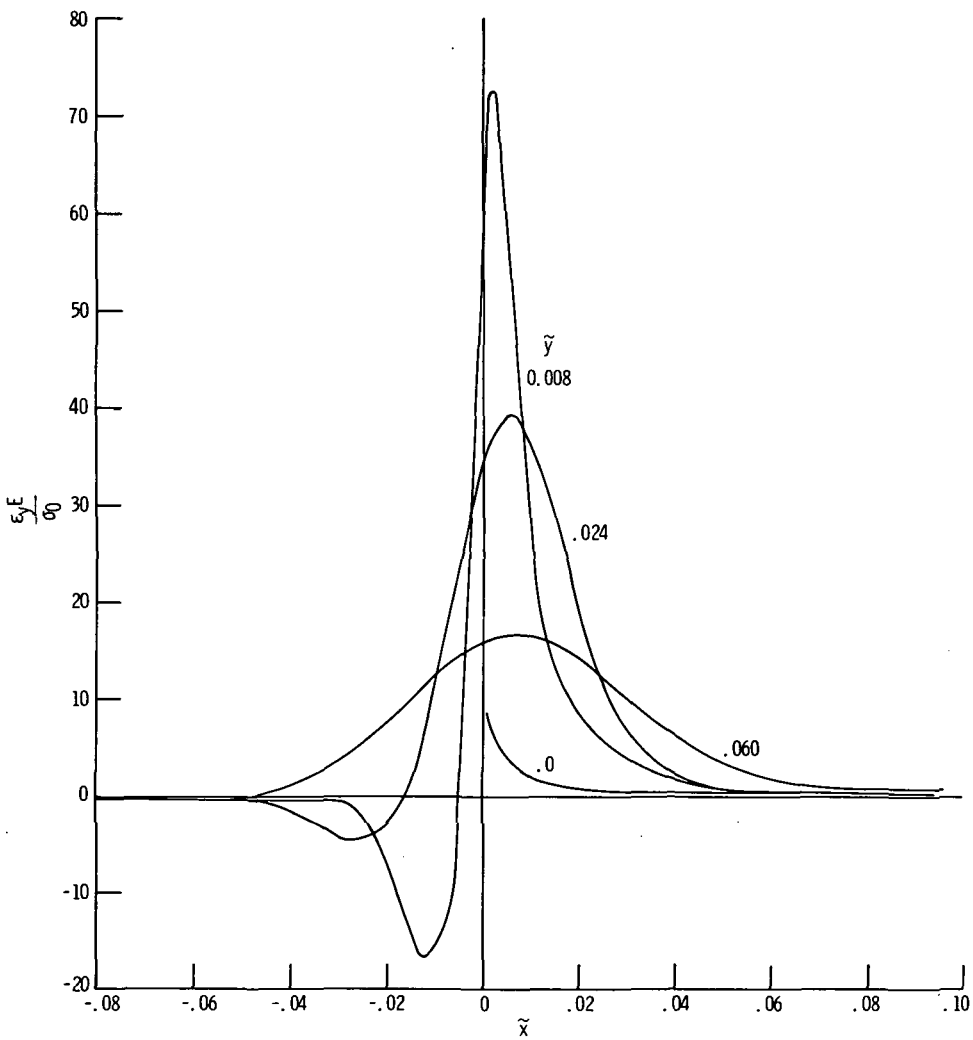

Figure 21. - Dimensionless y-directional total strain distribution along $\tilde{y}$ = constant lines in vicinity of notch for specimen with single edge notch subjected to pure bending. Plain strain; dimensionless load $\tilde{q} = 0.7$; dimensionless notch depth $\tilde{a} = 0.5$; notch angle $\alpha = 10^0$; strain hardening parameter $m = 0.05$; Poisson's ratio $\mu = 0.33$.

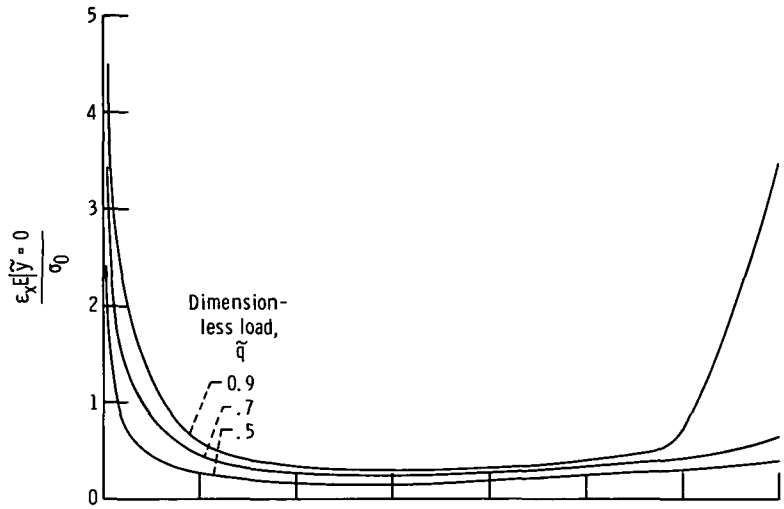

(a) Dimensionless x-directional total strain as a function of $\tilde{x}$.

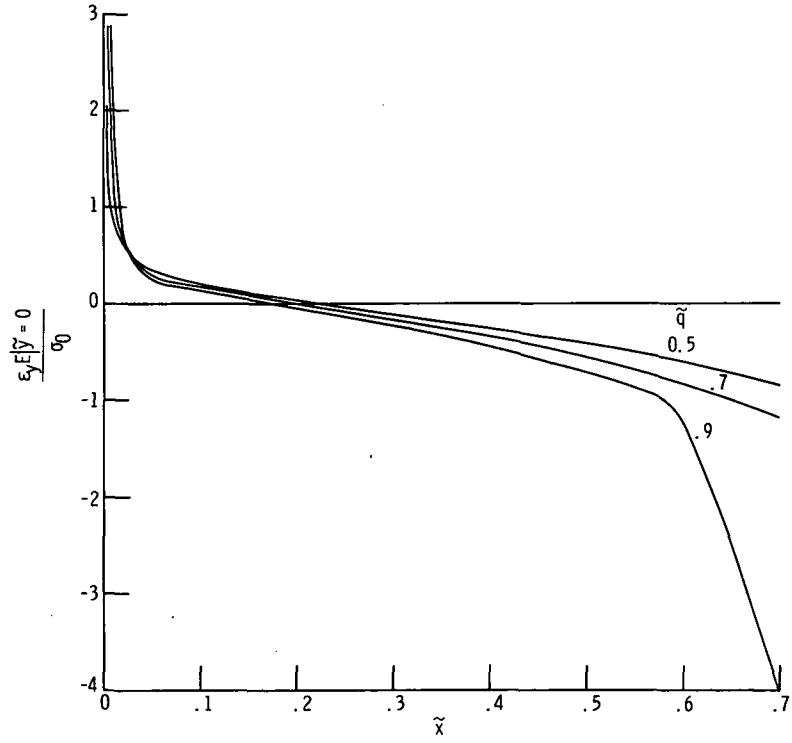

(b) Dimensionless y-directional total strain as a function of $\tilde{x}$.

Figure 22. - Dimensionless x- and y-directional total strain distribution along x-axis for specimen with single edge notch subjected to pure bending. Plane strain; dimensionless notch depth $\tilde{a} = 0.3$; notch angle $\alpha = 10^0$; strain hardening parameter $m = 0.10$; Poisson's ratio $\mu = 0.33$.

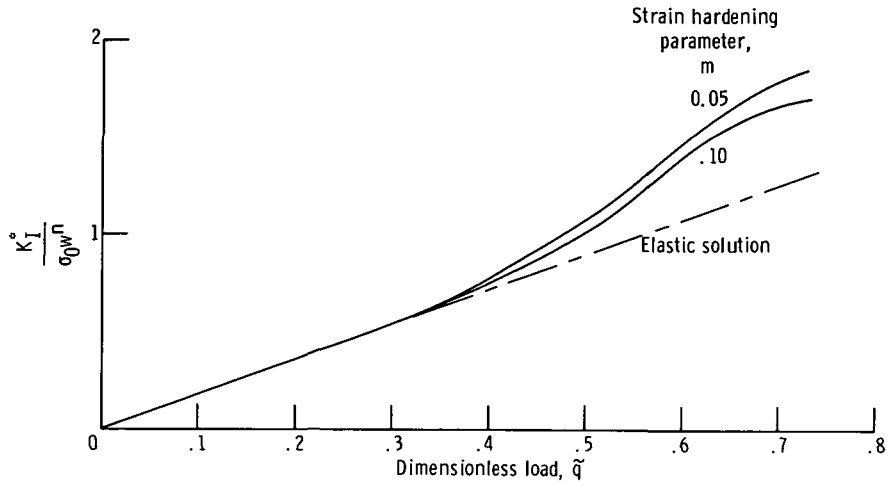

Figure 23. - Variation of dimensionless generalized stress intensity factor with load for specimen with single edge notch subjected to pure bending. Plane strain; dimensionless notch depth $\tilde{a} = 0.5$; notch angle $\alpha = 10^0$; Poisson's ratio $\mu = 0.33$.

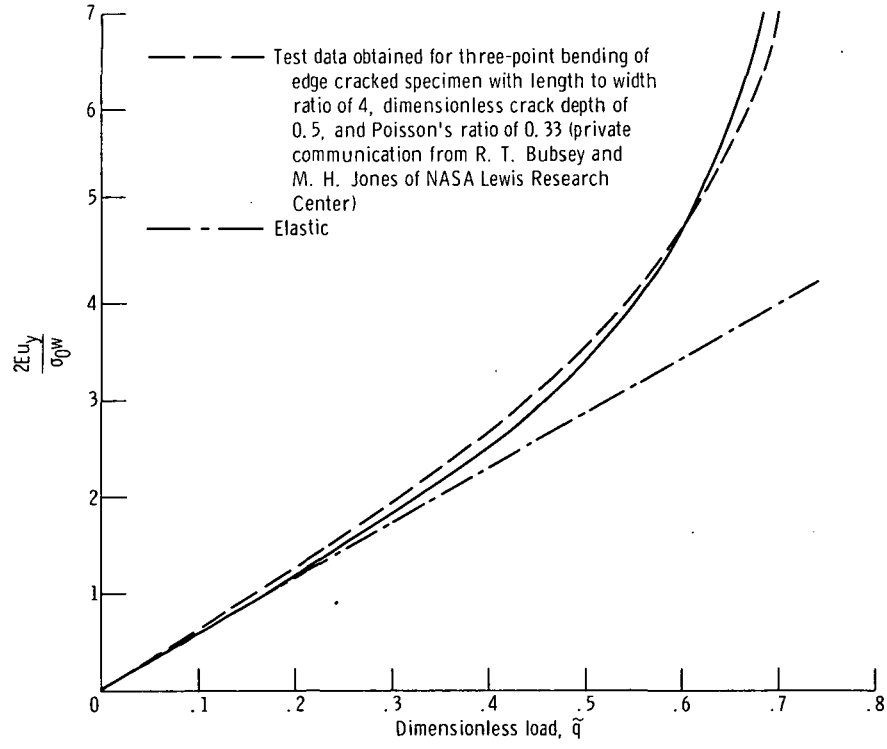

Figure 24. - Dimensionless plane strain y-directional notch opening displacement for specimen with single edge notch subjected to pure bending. Dimensionless notch depth $\tilde{a} = 0.5$; notch angle $\alpha = 10^0$; Poisson's ratio $\mu = 0.33$; stress-strain curve given by figure 25.

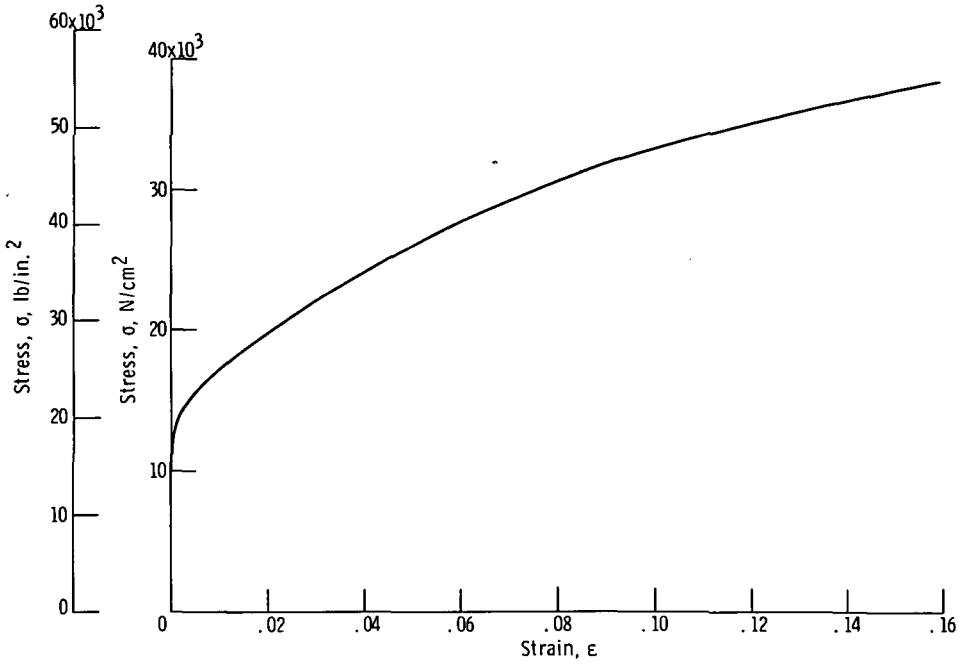

Figure 25. - Stress-strain curve for aluminum 5083-0 used in test (private communication from R. T. Bubsey and M. H. Jones of NASA Lewis Research Center). Young's modulus of elasticity $E = 7.79 \times 10^6$ newtons per square centimeter (11.3×10^6 lb/in.^{2}); Poisson's ratio $\mu = 0.33$.

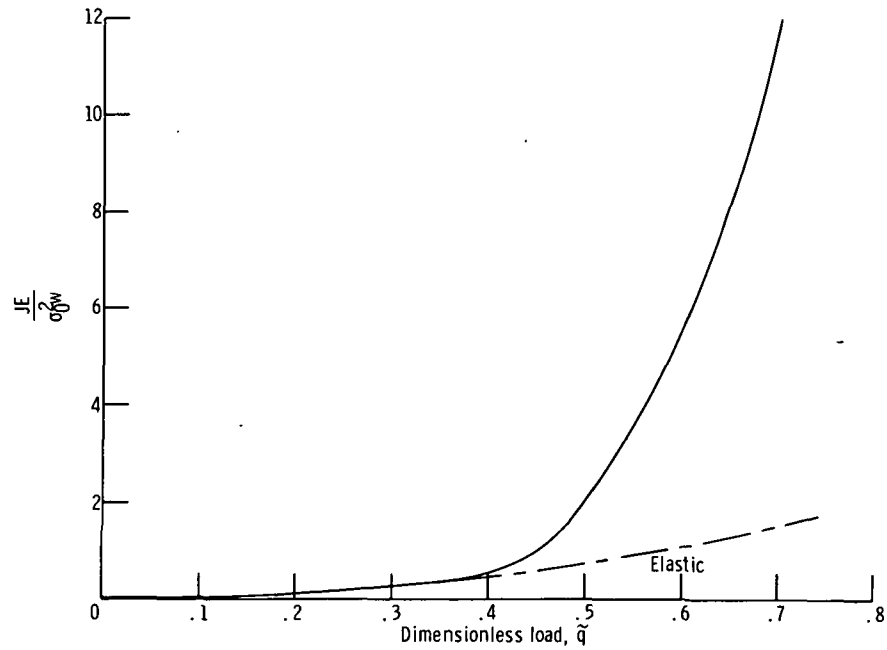

Figure 26. - Dimensionless plane strain $\tilde{J}$ integral for specimen with single edge notch subjected to pure bending. Dimensionless notch depth $\tilde{a} = 0.5$; notch angle $\alpha = 10^0$; strain hardening parameter $m = 0.05$; Poisson's ratio $\mu = 0.33$.

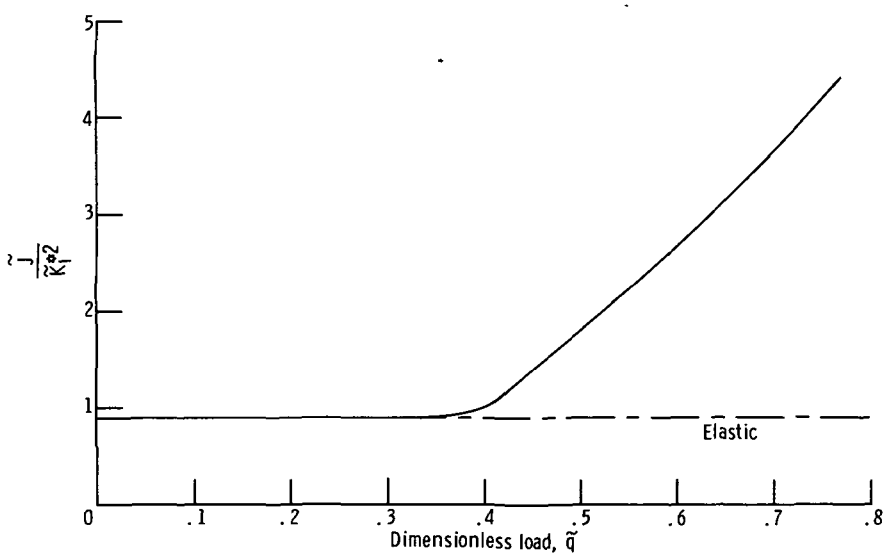

Figure 27. - Variation of ratio of dimensionless $\tilde{J}$ integral to square of dimensionless generalized stress intensity factor $\tilde{K}_I^{*2}$ with load for specimen with single edge notch subjected to pure bending. Plane strain; dimensionless notch depth $\tilde{a} = 0.5$; notch angle $\alpha = 10^0$; strain hardening parameter $m = 0.05$; Poisson's ratio $\mu = 0.33$.

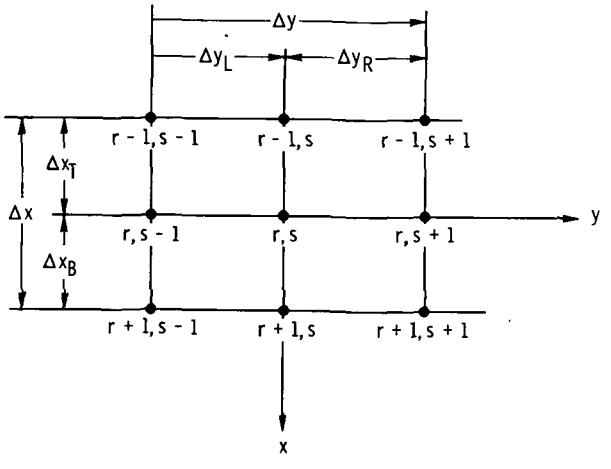

Figure 28. - Finite difference net for station (r, s).